LAWRENCE
LIVERMORE
NATIONAL
LABORATORY

UCRL-TR-224527

Virtual Crystallizer

T. A. Land, R. Dylla-Spears, C. B. Thorsness

September 19, 2006

Disclaimer

Auspices Statement

This work was performed under the auspices of the U. S. Department of Energy (DOE) by the University of California, Lawrence Livermore National Laboratory (LLNL) under Contract No. W-7405-Eng-48. The project (XX-XXX-XXX) was funded by the Laboratory Directed Research and Development Program at LLNL.

FY05 LDRD Final Report
Virtual Crystallizer
LDRD Project Tracking Code: 03-ERD-XXX
Teresa Land, Principal Investigator

ABSTRACT

Large dihydrogen phosphate (KDP) crystals are grown in large crystallizers to provide raw material for the manufacture of optical components for large laser systems. It is a challenge to grow crystal with sufficient mass and geometric properties to allow large optical plates to be cut from them. In addition, KDP has long been the canonical solution crystal for study of growth processes. To assist in the production of the crystals and the understanding of crystal growth phenomena, analysis of growth habits of large KDP crystals has been studied, small scale kinetic experiments have been performed, mass transfer rates in model systems have been measured, and computational-fluid-mechanics tools have been used to develop an engineering model of the crystal growth process. The model has been tested by looking at its ability to simulate the growth of nine KDP boules that all weighed more than 200 kg.

INTRODUCTION

The capability to predict how crystals grow is a valuable tool for any industry involved in commercialized crystal production. For example, companies making pharmaceuticals and crystals for optical components have a vested interest in being able to reproducibly grow crystals. To accomplish this we have developed a computer model capable of predicting growth from a 1 cm size seed to a large 60 cm crystal (a mass change of ~300,000) utilizing actual crystallizer system conditions. The "virtual crystallizer" model provides a way to do computer simulation and screening of various growth strategies. It can be used to:

1. An understanding of the sensitivity of growth to various parameters and how to use them effectively to control growth.
2. A method for optimizing growth conditions.
3. The ability to grow a crystal with desired dimensions and properties reproducibly.

Potassium dihydrogen phosphate (KDP) has long been the canonical solution crystal growth system and has been well studied by various techniques over the years [1-8]. Further, researchers at LLNL are recognized as leaders in the field of fundamental research on crystal growth, including growth of large 60-cm KDP crystals [3-8]. For these reasons, we have chosen the KDP system to benchmark the "virtual crystallizer" model. We feel that the combined knowledge of the fundamental physics of KDP crystal growth along with the ability to grow large crystals puts us in a unique position to both develop and validate the "virtual crystallizer" model.

The virtual crystallizer model has been developed based on our current understanding of the rate controlling processes. The key inputs are shown in the block diagram in Figure 1 and summarized below.

A. The fundamental physics and chemistry of crystal growth. These are incorporated via known equations governing growth. The effect of impurities (in this case aluminum) on the prism face growth are incorporated into the kinetic equations.

B. The effect of mass transfer to crystal faces. The mass transfer rates are a function of crystal size, platform/crystal rotation schedule, and properties of the solution.

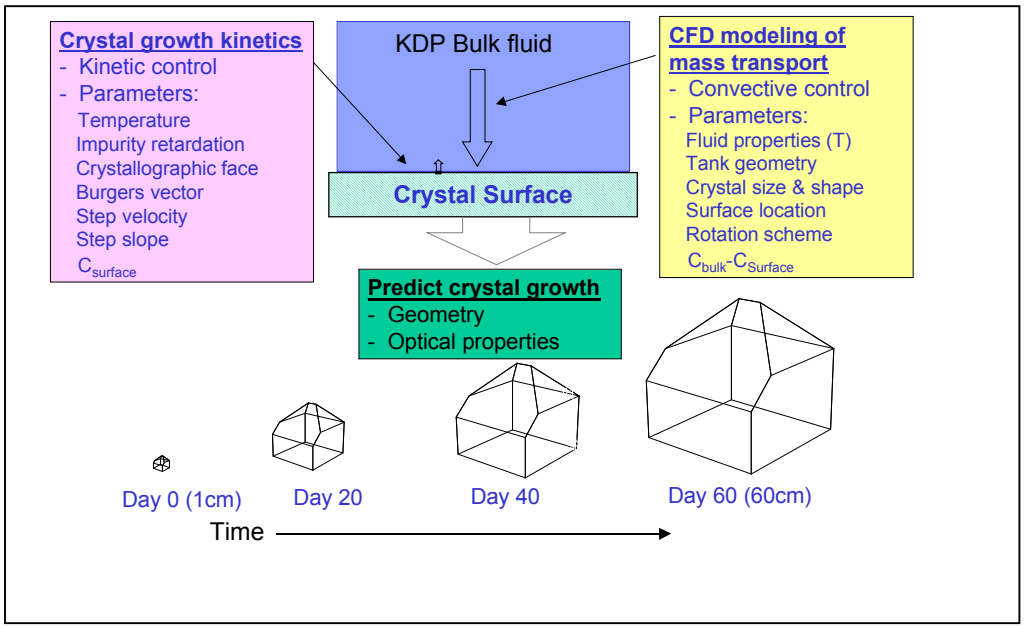

Figure 1. The key inputs to the virtual crystallizer model (components of mass transfer and kinetic parameters of growth) are shown in the boxes above. The output of the model will be growth curves for each face that will be used to generate a 3D crystal as a function of growth conditions and time.

The model translates all the key inputs described above into a large-scale crystal growth model that calculates growth rates for the individual faces and allows them to evolve in time to form a 3D crystal. The set of nonlinear differential/algebraic equations resulting from the mathematical representation of the system are solved using DASSL, a state-of-the-art software package capable of solving index one problems. Model variables include total volume, solution concentration, temperature, and impurity level. The output of the model is a set of growth curves for each face and the 3D geometry of the crystal as a function of time and growth conditions.

Fundamental physics and chemistry of growth

KDP is a complex but well studied system [1-8]. Growth occurs on two faces, pyramidal and prismatic. Based on microscopic scale studies these faces have been shown to grow very differently from each other and their growth rates vary in a complex way with supersaturation. Figure 2 shows the two faces and highlights the differences and Fig. 3 shows plots of how the growth parameters for each face are affected differently by supersaturation. In addition, growth (step velocity) on the prismatic face is very sensitive to the presence and level of certain elements which exist as impurities in the growth solution. Adding to the complexity are the effects of temperature on the kinetics of step growth and impurity incorporation both of which intimately effect step velocity and overall growth rates. In order to grow a crystal with the desired shape it is critical to be able to control the relative growth rates of the two faces during the growth run. Since the "virtual crystallizer" model includes kinetics governing growth of the KDP system and allows us to determine the sensitivity of growth to the various parameters. This enables us to use the model to judiciously choose conditions (i.e. supersaturation and rotation parameters) to control the growth rates and achieve the desired crystal dimensions.

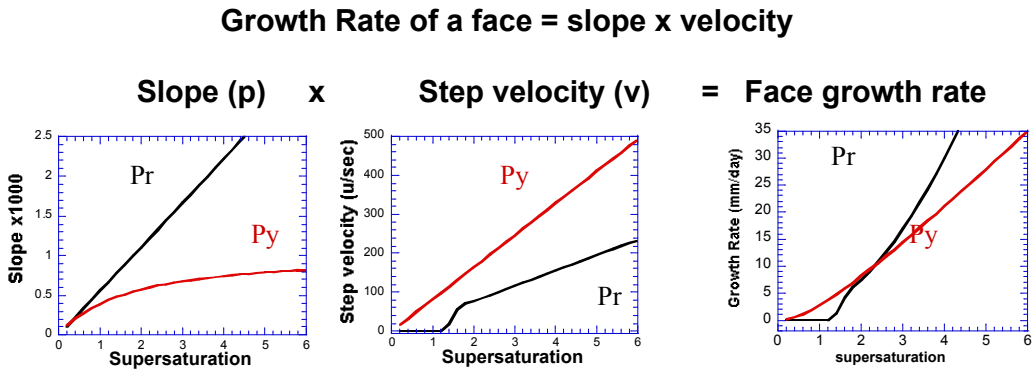

Figure 2. Growth of KDP occurs on two faces, pyramidal and prismatic which grow very differently from each other. The cartoon at the left shows the two faces and the AFM images and text highlight the differences between them.

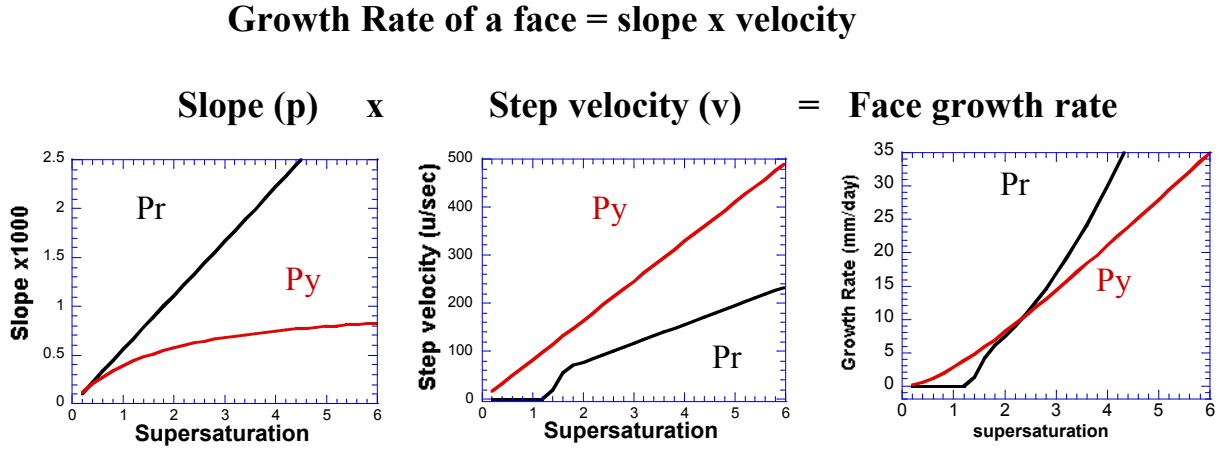

Figure 3. These plots show how the fundamental growth parameters for each face are affected differently by supersaturation. In addition, growth (step velocity) on the prismatic face is very sensitive to the presence and level of certain elements which exist as impurities in the growth solution as seen in the region of zero velocity on the prismatic face. The equations containing the fundamental physics of growth will be incorporated into the model.

Mass transfer

Mass transfer is a key component of crystal growth physics as it governs the supersaturation and thus the material available to feed a crystal face. Controlling supersaturation at the crystal face affects the relative growth rates of each face and consequently, the crystal aspect ratio. In a real crystallizer, mass transfer to the crystal face varies as a function of position on the face and the rotation schedule. The crystal is on a platform that is rotated through the solution at various schedules during the run. The rotation cycle has four components: acceleration, velocity, period at constant velocity and pause. The rotation cycle, shown in Fig. 4, begins with the platform at rest for two seconds, then accelerates to a constant velocity, continues at constant velocity for a period of time, decelerates, pauses for two seconds then begins the cycle over again in the reverse direction. The acceleration, constant velocity and the period at constant velocity vary during the course of the growth run. CFD modeling [11] has suggested that the supersaturation can vary across the crystal face as shown in shown in Figure 4. Similarly, mass transfer to the face also varies with increasing size of the crystal and temperature of the system [11]. Typically the temperature changes from 75-20C during a growth run. This change in temperature in turn affects the properties of the fluid. During a growth run, as the crystal gets larger other changes occur. The larger the crystal the more it begins to act like a paddle and agitate the solution causing a large turbulent surface wave in the crystallizer. This turbulence in turn causes splashing of the solution onto surfaces in the headspace above the solution. If these surfaces are too hot or too cold, the droplets condense and can become sites for nucleation. Secondary nucleation is the primary cause of growth run failure and needs to be understood to be successful in growing crystals. Along with splashing, the stress induced on the crystal by the rotating platform can result in the generation of small flakes off the crystal that serve as nuclei.

As the crystal becomes larger and the force from acceleration becomes greater this exacerbates stress risers in the crystal that cause small fragments to break off.

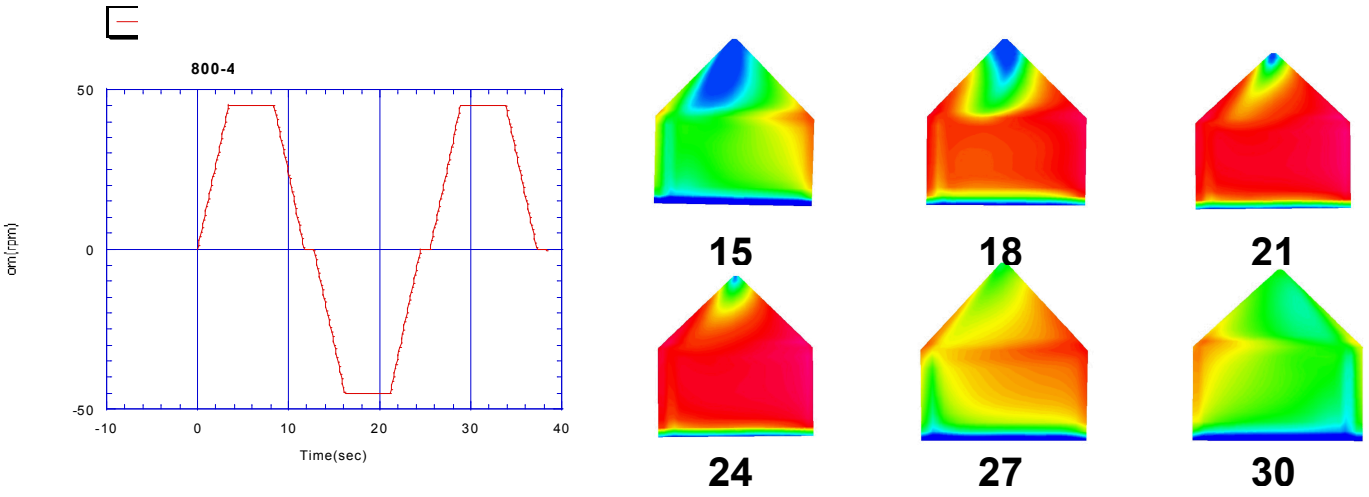

4a. 4b.

Figure 4. a.) Shows the four basic components of the rotation schedule: acceleration to a constant velocity, rotates for a period of time at constant velocity, decelerates, pauses and begins the cycle again in the opposite direction. b.) CFX 5.1, from AEA Technology Engineering Software has the capability to solve complicated systems of mass, momentum and energy equations. It also has a capability to visualize and analyze the results. The images show an example of how mass transfer to the crystal face can vary as a function of position on the face and the rotation schedule. (Red is the highest supersaturation and blue is lowest).

To minimize solution surface turbulence and stress on the crystal as it gets larger, the rotation schedule must be continually adjusted. In making this adjustment it is critical that the effect of the rotation schedule on the surface wave be balanced with providing adequate mass transfer to the crystal face. It is important to find a rotation schedule that provides as uniform mass transfer across the face as possible. Variations in supersaturation results in steps moving with different velocities. This can lead to step bending and entrapment of solution forming what is called solution inclusions [3,4,9,10]. Solution inclusions have a deleterious effect on the overall crystal quality and effect the optical transmission. Computational fluid dynamics modeling (CFD) has been used to help define rotation schedules that provide optimum mass transfer.

A typical 60-cm crystal growth run lasts about two months. During that time the crystal grows from 1-centimeter to 60-centimeters (a mass change of ~300,000), the temperature changes from 75-20°C and the rotation schedule is varied multiple times. These growth runs, which cover a range of temperature and growth conditions, and require a long time scale, provide an excellent test of the capability of the virtual crystallizer model to translate the fundamentals of growth to a large crystal.

Growth runs have been used to:

1. Validate use of the “virtual crystallizer” model to predictably grow a crystal of a desired size and shape

2. Ensure that the modeled rotations minimize solution surface turbulence (growth runs will provide feedback to the model on acceptable rotations in the real system and the presence or absence of secondary nucleation)
3. Validate that the modeled rotation schedule provides adequate mass transfer to the surface (demonstrated by inclusion-free growth)

Basic components of the actual crystallizer system

The actual crystallizer system, shown in Fig. 5, consists of a 1000L growth tank containing the KDP salt solution surrounded by a water bath that is used to control the temperature. An auxiliary tank can be used to provide any additional solution that allowing the temperature regime for crystal growth to be changed. Inside the growth tank the crystal grows on a rotating platform.

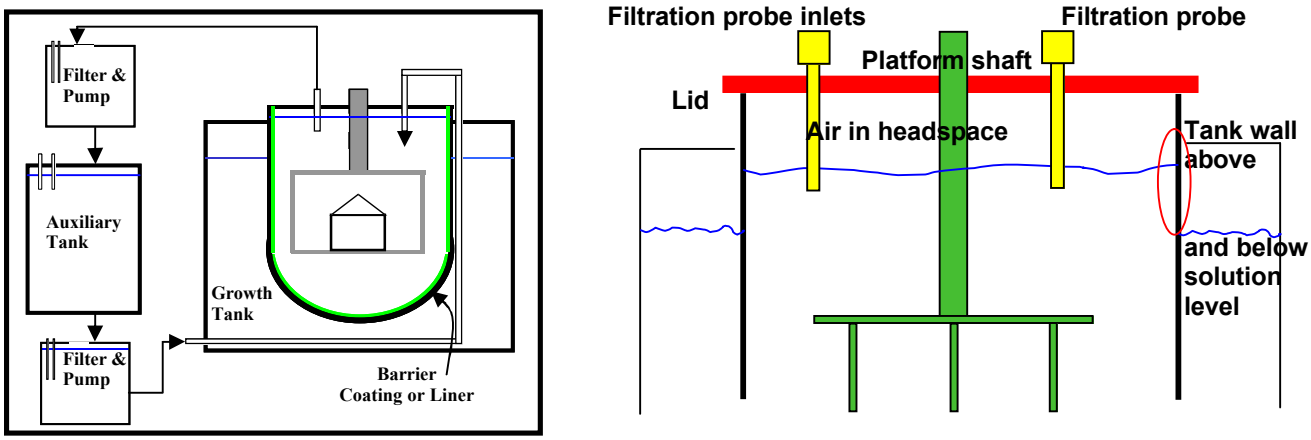

Figure 5. The cartoon shows basic components of the real crystallizer system. The system consists of a 1000L growth tank containing the salt solution surrounded by a water bath that is used to control the temperature. An auxiliary tank is used to provide any additional solution that is required to grow DKDP crystals. Inside the growth tank the crystal grows on a rotating platform. The cartoon at the right is a blow up of the head space region above the solution where we will measure the temperature gradients.

The platform is rotated as a means of agitating the solution to generate shear across the crystal face thus facilitating mass transfer of salt to the growing crystal. In the KDP system temperature is used to control the supersaturation and hence the growth rates. During a growth run the temperature of the system is typically lowered from 75°C to 20°C, with accuracy on the order of 0.1°C to maintain the desired growth rates. This makes thermal stability and control in the system imperative.

FLUID DYNAMICS RESULTS

The computational fluid dynamics (CFD) modeling focused on four test cases: 30 cm and 60 cm crystals each at two rotations. Initially, a mass transfer based approach to simulation was used. However, this model predicted unreasonably low mass transport. These results were not supported by experimental validation performed at NASA Ames

Research Center nor by growth run data. The CFD model has been modified to use the heat transfer equation, and results are now reasonably consistent with experiment and growth data. CFD simulation and experiment predict by heat transfer analogy that approximately 60% of the bulk supersaturation is present at the crystal surface due to mass transport limitations. Additional physical and numerical experiments are required to better understand mass transport sensitivity.

The CFD model that was developed in FY03 utilized the scalar transport equation, simulating KDP transport to the crystal surface. Under the same growth conditions, the results of the FY03 model compared qualitatively to earlier CFD models [13,11,14]. This model relied on a natural convection argument to bring simulated results into a physically meaningful regime. A minimum concentration was imposed as a post-simulation correction to the CFD-predicted results.[14]

Results from the scalar transport-equation based model were obtained for the four test cases using transport parameters, system temperatures, and growth parameters specific to each case. Even with the natural convection correction imposed, the numerical results provided unreasonably low mass transfer coefficients (Case 1: 1.6×10^{-5} m/s, Case 4: 0.4×10^{-5} m/s), implying that mass transport resistance allows only 10-30% of the bulk supersaturation to reach the crystal surface.

The scalar transport-equation-based CFD model yielded mass transport coefficients that are unreasonably low when compared to 1) growth run observations, 2) analyses from the crystal growth kinetic model (see section "Crystal Growth Kinetic Model"), and 3) results from experimental validation experiments performed at NASA Ames Research Center. In light of these conflicting results, focus in FY04 was shifted to obtaining a better understanding of the mass transfer situation. Until this is resolved, study of inclusion formation and parameter optimization is futile.

Experimental determination of mass transfer coefficient

NASA Ames Research Center was tasked with providing an experimental measure of the mass transport to the surface of a mock crystal. This was accomplished indirectly using a heat transfer analogy to mass transfer in a half-scale system. Boundary and initial conditions have been chosen to match the hydrodynamics of the full-scale crystallizer. Therefore, mass transfer results can be derived from heat transfer results using the Chilton-Colburn correlation. A constant heat flux is applied to the faces of a mock crystal. The temperature distribution at the crystal surface resulting from heat transport into the surrounding fluid is recorded as a function of time using CCD cameras and temperature-sensitive paint. Heat transfer coefficients are calculated from the temperature distributions, and the heat transfer coefficients are converted to equivalent mass transfer coefficients using the Chilton-Colburn correlation.

$$\frac{(k)_F}{h_M} = \frac{1}{(\rho c_P)_M} \frac{L_M}{L_F} \frac{\nu_F}{\nu_M} \left(\frac{Pr_M}{Sc_F} \right)^{2/3}$$

Equation 1. Chilton-Colburn correlation, where F represents full scale and M represents the model. k and h are the mass and heat transfer coefficients, respectively. L is the length scale, ν is the kinematic viscosity, Pr is the Prandtl number, and Sc is the Schmidt number.

These experiments have provided mass transfer coefficients for the four test cases examined using CFD. The spatially averaged mass transfer coefficients averaged over several rotation cycles were 2.2×10^{-5} m/s for a 30 cm crystal and 1.1×10^{-5} m/s for a 60 cm crystal. This implies that, due to mass transfer limitations only about 60% of the bulk supersaturation is present at the crystal surface for both 30 cm and 60 cm crystals. The NASA results showed that for a given crystal size, rotation rate made little difference in mass transfer coefficient. This surprising result from the limited data set warrants further experimental investigation.

Results of revised heat transfer-based CFD model

The CFD was been revised to study the exact heat transfer problems used in the NASA experiments. As in NASA's experiments, temperature distributions along the crystal surface are converted to mass transfer coefficients. The new heat transfer CFD model was used to understand mass transport to the crystal using the four tests cases examined previously. The heat transfer CFD simulations predict mass transport coefficients two times larger than did the previous scalar-transport CFD model. The results are in line with results from NASA experiments and from exploration of the crystal growth kinetic model. The simulations produce spatially averaged mass transfer coefficients of 2.9×10^{-5} m/s for a 30 cm crystal (Case 1) and 1.1×10^{-5} m/s for a 60 cm crystal (Case 4) when averaged over several rotation cycles. This implies about 70% of the bulk supersaturation reaches the crystal surface for 30 cm crystals and only 50% reaches the surface for 60 cm crystals.

Figure 6 shows maps of time mass transfer coefficient time averaged over rotation cycle predicted by experiment and by CFD for Case 1 (30 cm). Data from experiment compares reasonably well with the results of CFD numerical simulation. The two data sets show strikingly similar patterns across the crystal face, with little spatial variation across the prism on average. In addition to the results shown in figure 1, we also see a difference between the two where the CFD model results show variation with rotation change for crystals of the same size where the experimental results from a limited data set is not showing this variation.

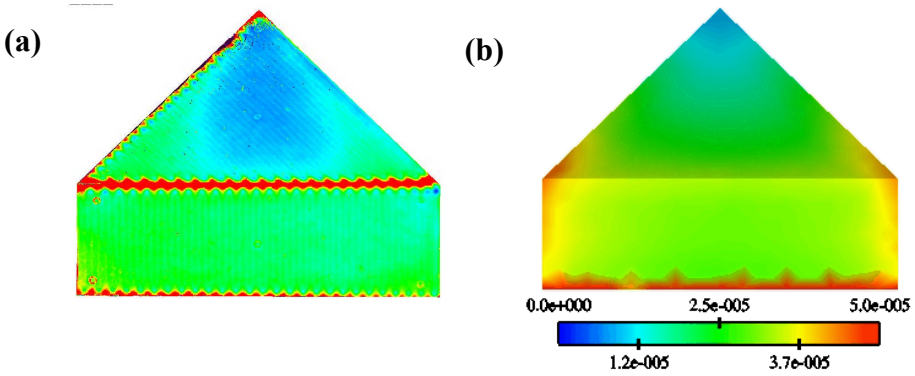

Figure 6. Maps of average mass transfer coefficient in m/s for Case 1 (30 cm crystal at 500-50-20-2) determined by: a) heat transfer experiment, b) heat transfer CFD simulation. Scale applies to both pictures.

The results of both the NASA experiment and the CFD numerical simulation are of the same order as predicted by growth run data and suggest that mass transport does play a role, but not dominant role, in determining crystal growth rate.

CRYSTAL GROWTH

Over the last year a series of large KDP crystals have been grown in Teflon (FEP) lined growth tanks. The lining removes the problem of glass dissolution into the growth solution. This dissolution made control of the exact chemical composition of the growth solution problematic. Since crystal growth habit is a function of trivalent cation concentration and the glass contained significant quantities of trivalent aluminum, determining the influence of process variables on growth geometry was difficult.

In examining these runs we found that there was a considerable variability in crystal shape, even though nominally similar process conditions were employed. These different shapes are a result of the variability in face growth velocities seen on different crystal faces during a run. We attribute this variability to the strength and/or location of the dominant dislocations on each face. Dislocation position, strength and supersaturation levels determine the face velocities that are present in a run. The source location is primarily important in determining the average mass transfer characteristics that interact with the source strength to determine growth velocity. The source strength variability inferred from the large boule data is less than what we have seen in our kinetic experiments using small (5mm) crystals. The reduced variability is probably a result of the mass transfer's smoothing influence and the fact that the face velocity is only dependent on the activity of the most active source.

We find that after ~10 days of a typical 45-day run the shape of the crystal is established. That is, the final crystal for the most part looks like an enlarged version of the small crystal. This shape consistency is attributed to the fact that relative face velocities do not very greatly over the course a run. This implies that the controlling sources remain dominant during the entire run and changes in mass-transfer behavior with crystal size are not large enough to unduly influence the relative growth rates. A consequence of congruent growth geometry is that it is possible to make meaningful predictions about ultimate optical plate yields from a boule after ~10 days.

A final observation is that relatively modest variations in face growth velocities (10%) can yield different looking crystal shapes. Since these variations appear to be random, it is nearly impossible to draw conclusions about the influence of changes of operation conditions on growth habit of large crystals on the basis of one or two experiments.

In the following we first present run data from eleven KDP production runs in lined tanks. This includes wire-frame representations of crystal shape as a function of time, extensive plots of prism position and heights as well as prism and pyramid velocities computed from these positions. This is followed by analysis of the data aimed primarily at quantifying the degree of invariability of crystal shape and outlining a method of estimating optical plate yield from early growth data.

Data

In the recent series of lined-tank production growth runs similar growth conditions have been employed, with the exception of aluminum concentration in the growth solution. All runs started at a temperature of just over 70°C and most terminated near 20°C. Growth rates were controlled by using a target vertical growth rate. This rate was set at ~10 mm/day until the crystal reached a mass of approximately 125 kg and then was dropped linearly to a value of 2.4 mm/day at 300 kg. Most runs were terminated before reaching 300 kg. Termination for the most part was a result of the crystals growing off the platform.

Summary Data: Summary run data is listed in Table 1. Included in the data are estimates for the theoretical number of 14.1 mm NIF size (42 × 42 cm) doubler or SHG (second harmonic generator) plates that can be cut from the produced boules. We see that all the listed crystals, with the exception of E-21 (no aluminum run), can theoretically produce doubler plates.

Table 1. Summary data.

Run	Days	Mass(kg)	Start T(C)	End T(C)	Width(cm)	Height (cm)	Aspect Ratio	14-mm SHG Plates
B-15	49	265	73	23	64	47	0.74	4
C-46	50	288	74	12	63	48	0.76	5
C-47	43	278	76	24	63	50	0.79	8
E-15	47	268	73	16	62	47	0.76	5
E-17	48	279	75	21	59	47	0.80	5
F-21	49	295	75	15	63	50	0.80	9
F-22	46	268	75	24	60	51	0.85	6
C-48	47	286	75	17	63	49	0.78	9
B-17	48	285	74	15	60	53	0.88	10
C-49	53	290	74	13	58	55	0.96	5
E-21	32	199	75	43	62	39	0.62	0
Average	47	273	74	20	61	49	0.79	6.0

All runs begin with a seed crystal. This seed crystal is partially dissolved prior to starting a run. This process of dissolving the seed and generating clear crystal growth is called a re-generation. All but one of the runs reported here started with a rectangular

parallelepiped seed that was 1.6cm wide and 0.8-cm high. After regeneration the initial fully formed crystal generally had a width on the order of 2 cm with a similar height. There were two exceptions to this general stating condition: Run C-48 used a tall seed, approximately 4cm high; and run E-21 underwent multiple re-generation procedures yielding a starting crystal width of about 5cm.

***Crystal Shape*:** During nine of these 11 runs each of the four prism heights were recorded at regular intervals. This information along with the two crystal-width dimensions, routinely recorded, allows the crystal geometry to be known as a function of time. Six independent dimensions are required to completely specify the crystal shape, as long as the small anti-pyramidal faces that often develop at the crystal base are disregarded. These measurements were used to generate the time dependent crystal shapes shown in Figs. 7-15. The crystal shapes are shown at roughly 15 kg intervals in crystal mass.

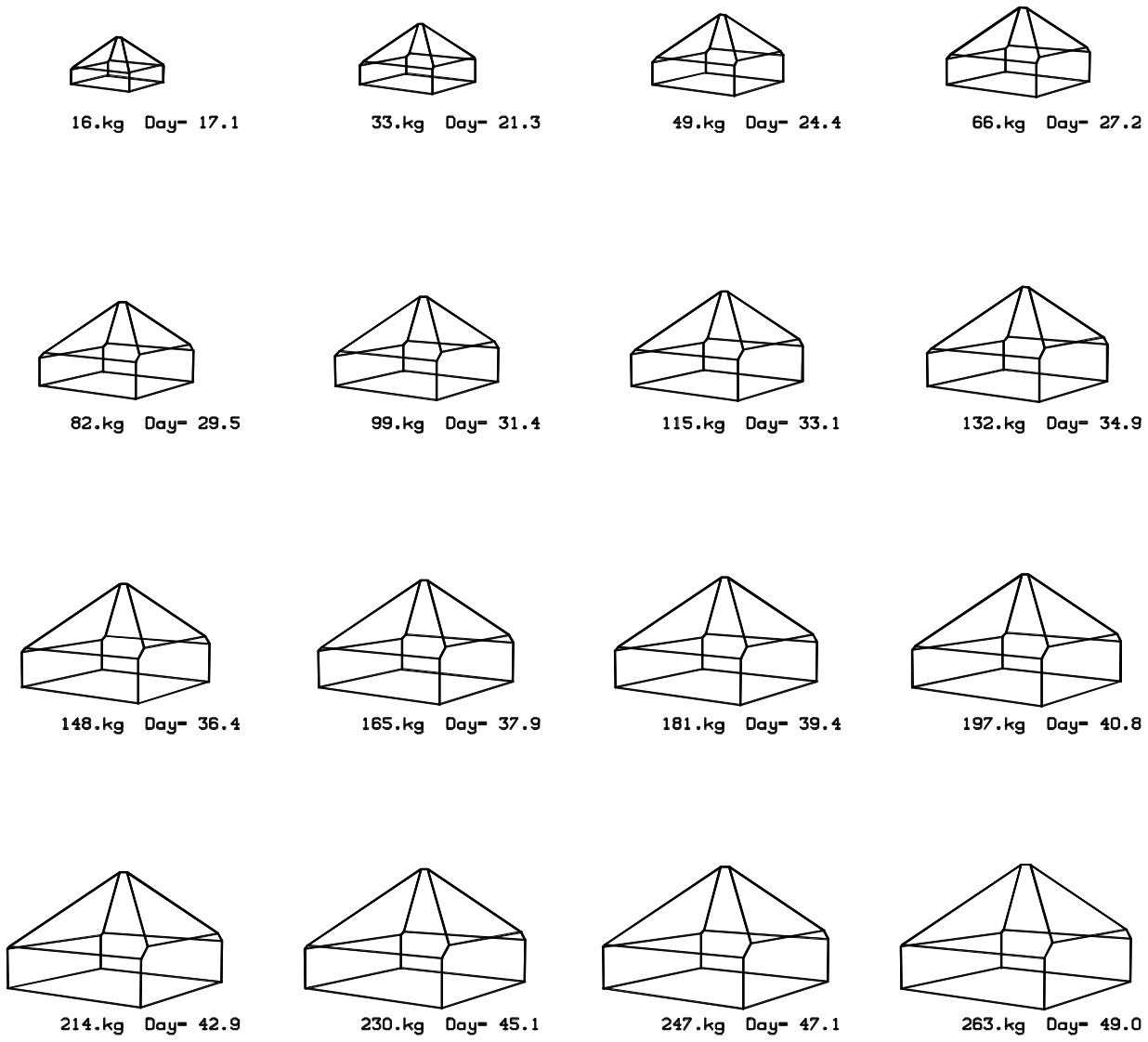

Figure 7. B-15 crystal shapes as a function of time.

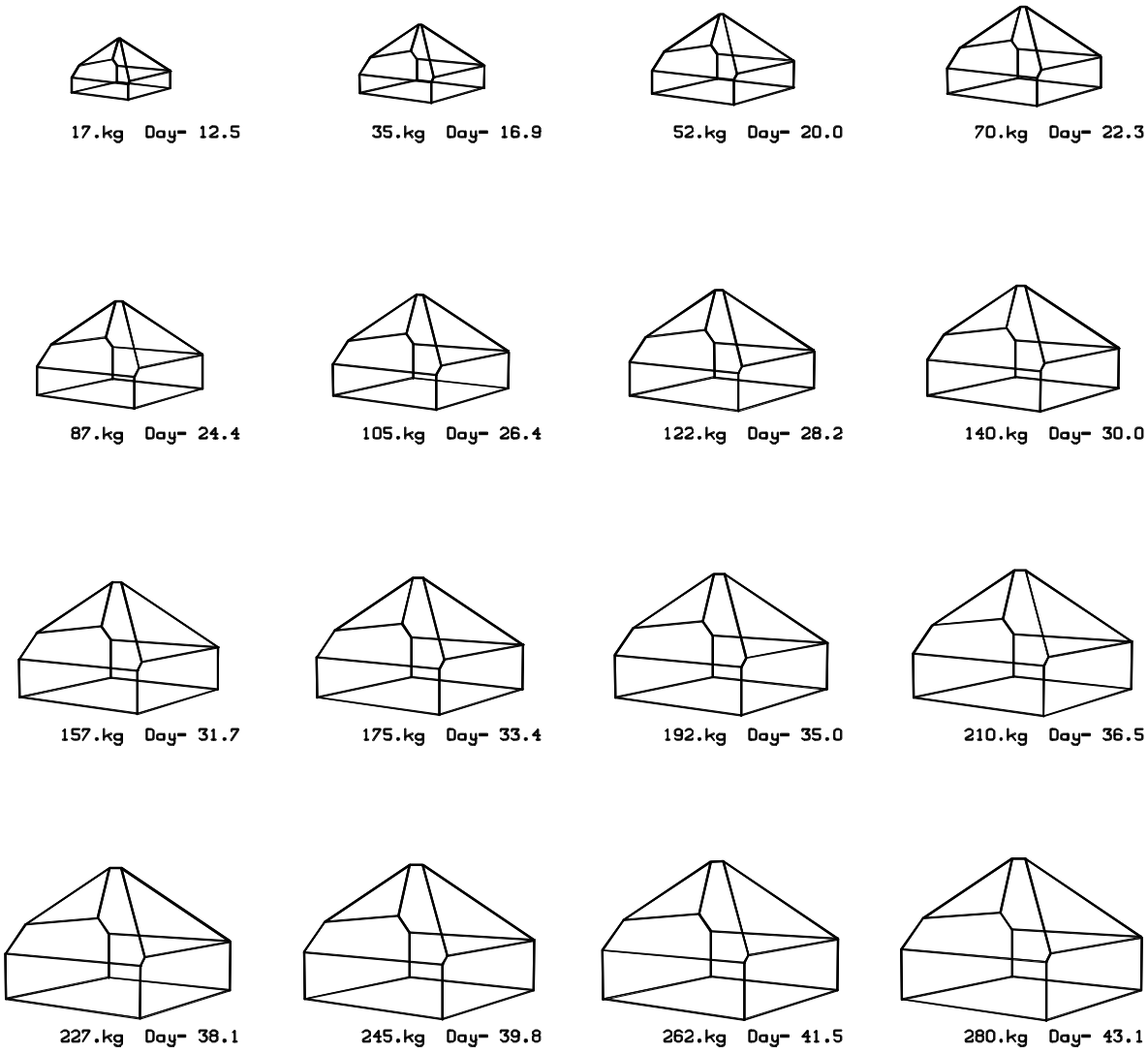

Figure 8. C-47 crystal shapes as a function of time.

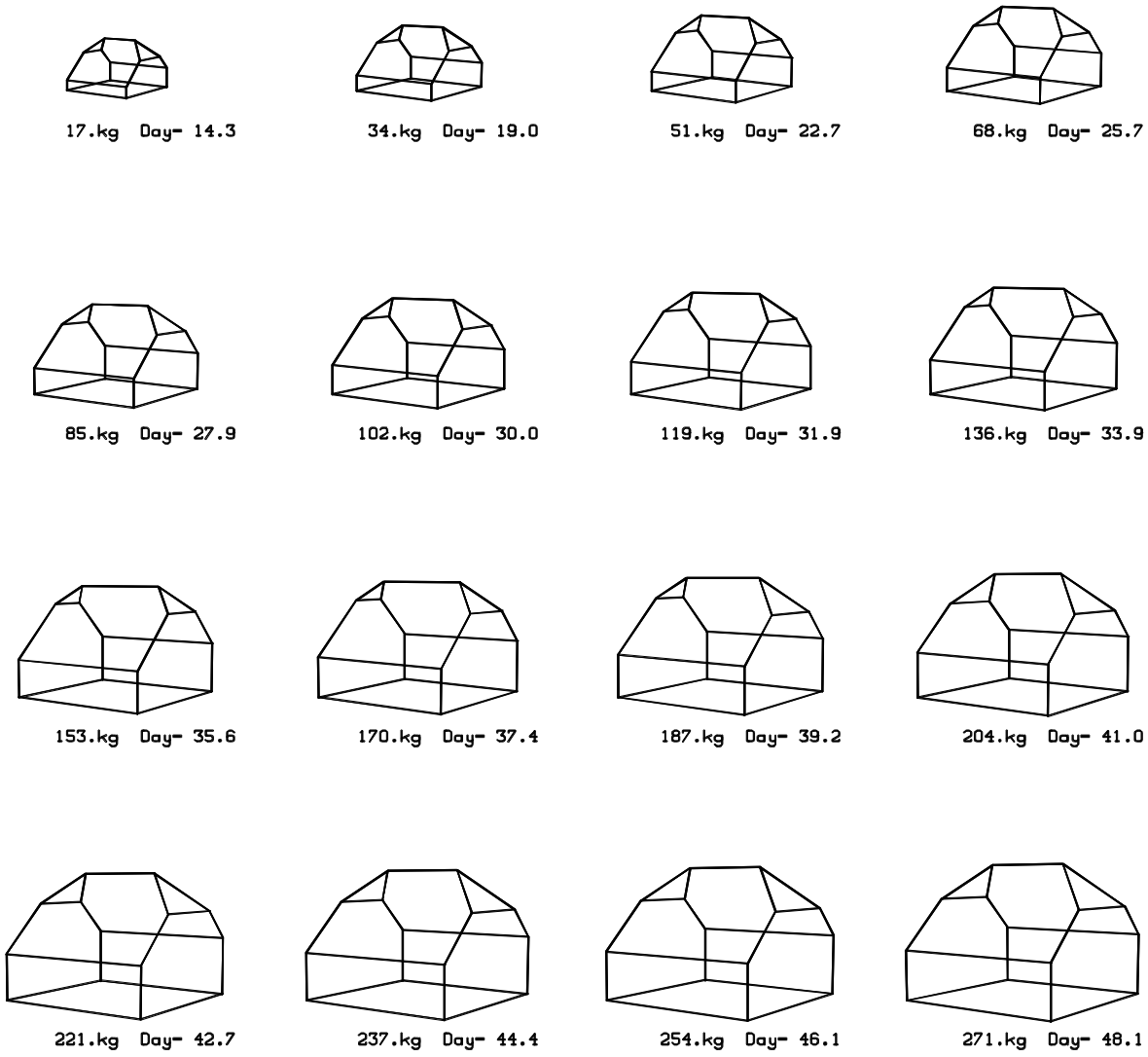

Figure 9. E-17 crystal shapes as a function of time.

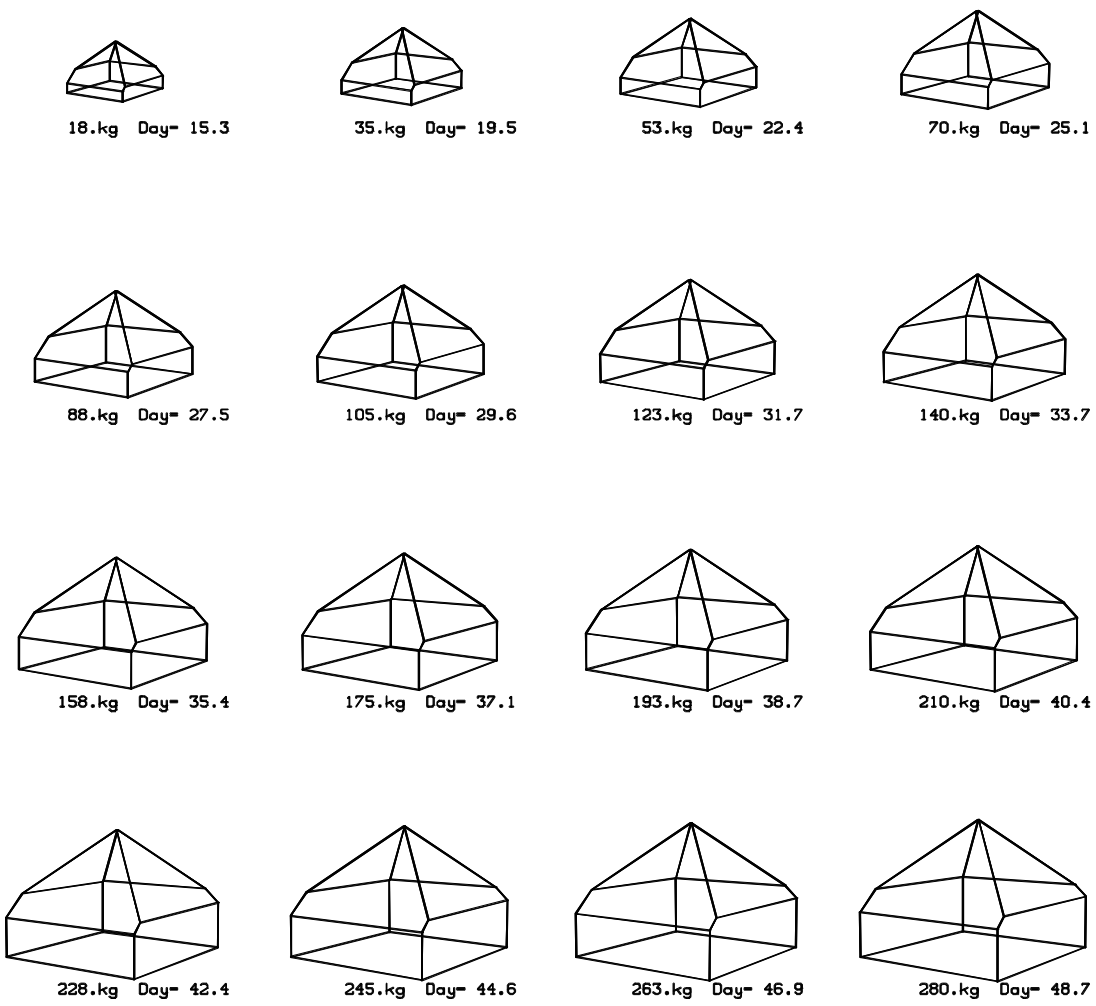

Figure 10. F-21 crystal shapes as a function of time.

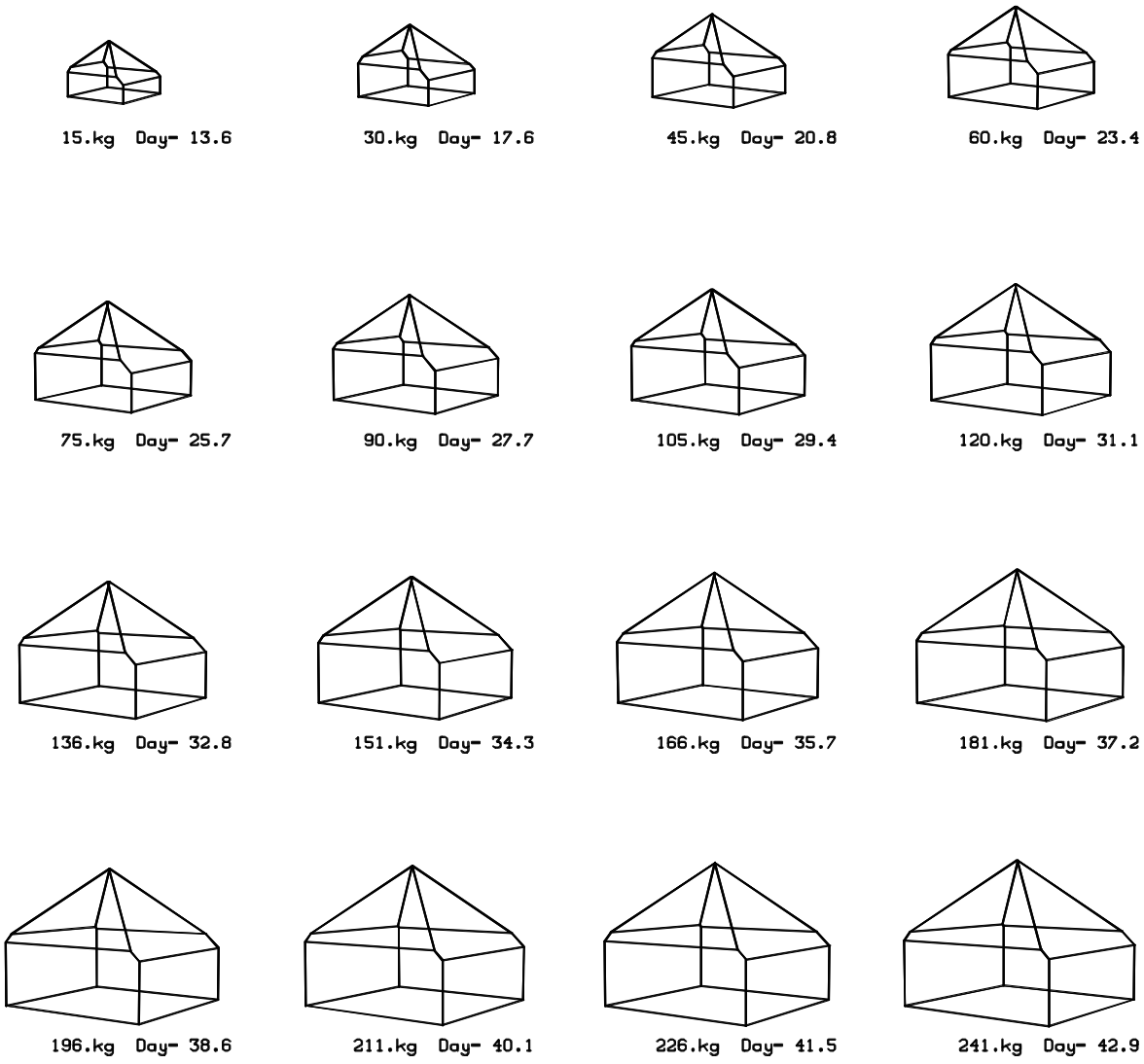

Figure 11. F-22 crystal shapes as a function of time.

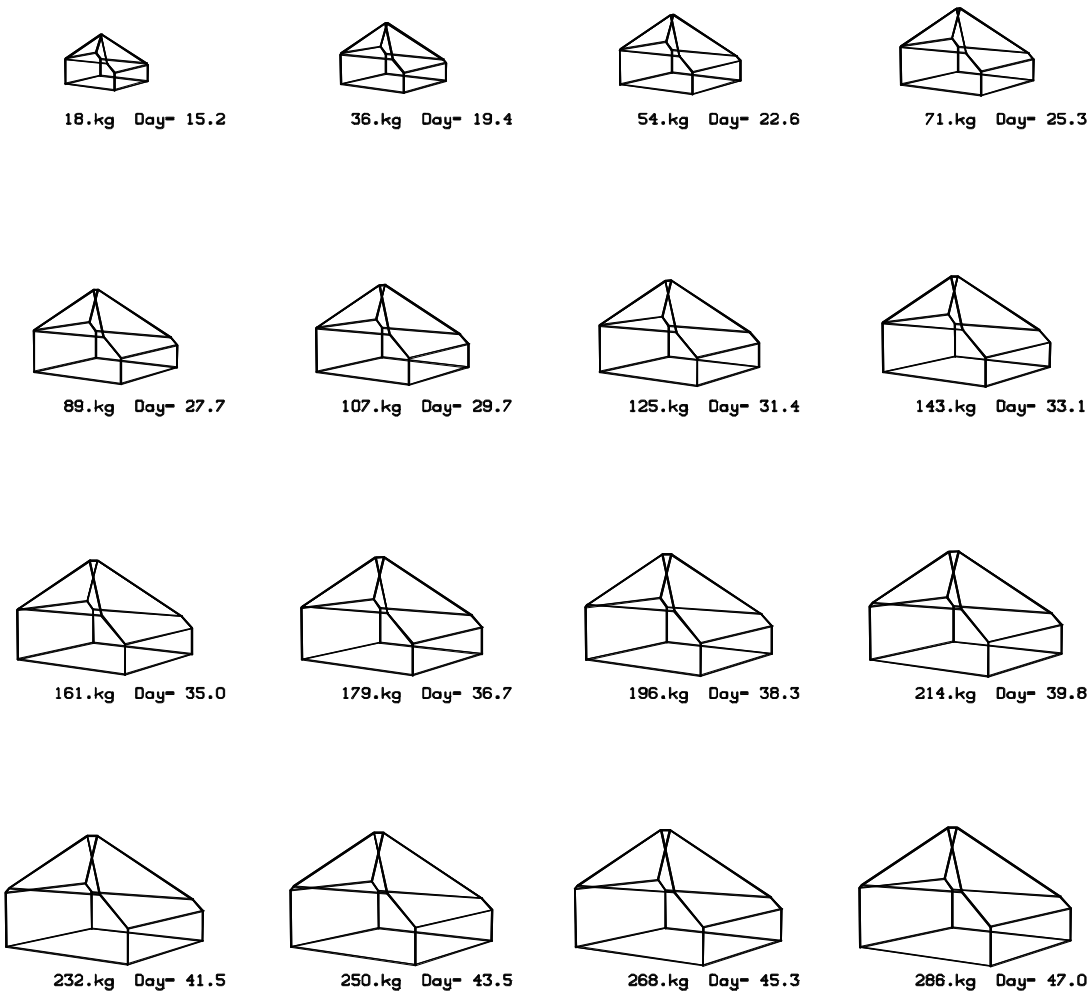

Figure 12. C-48 crystal shapes as a function of time.

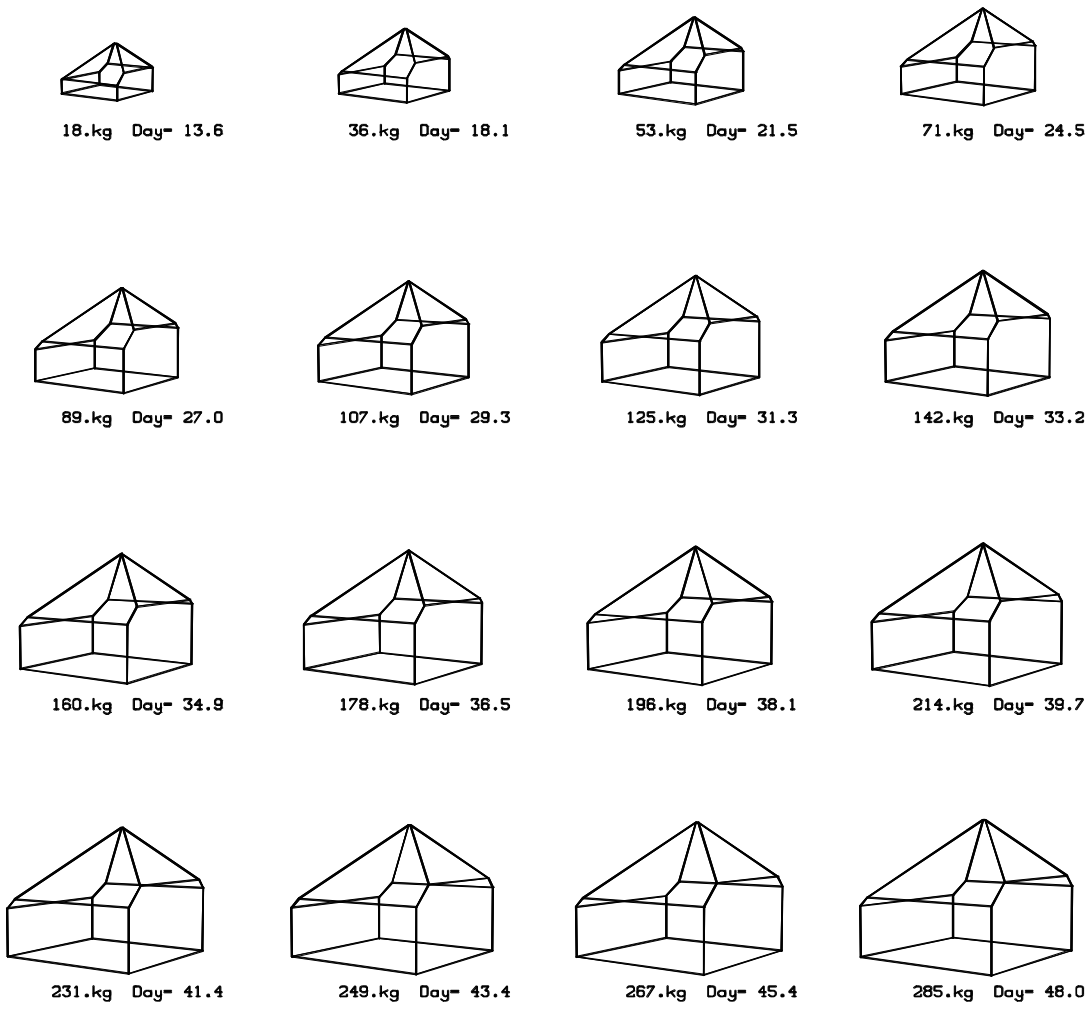

Figure 13. B-17 crystal shapes as a function of time.

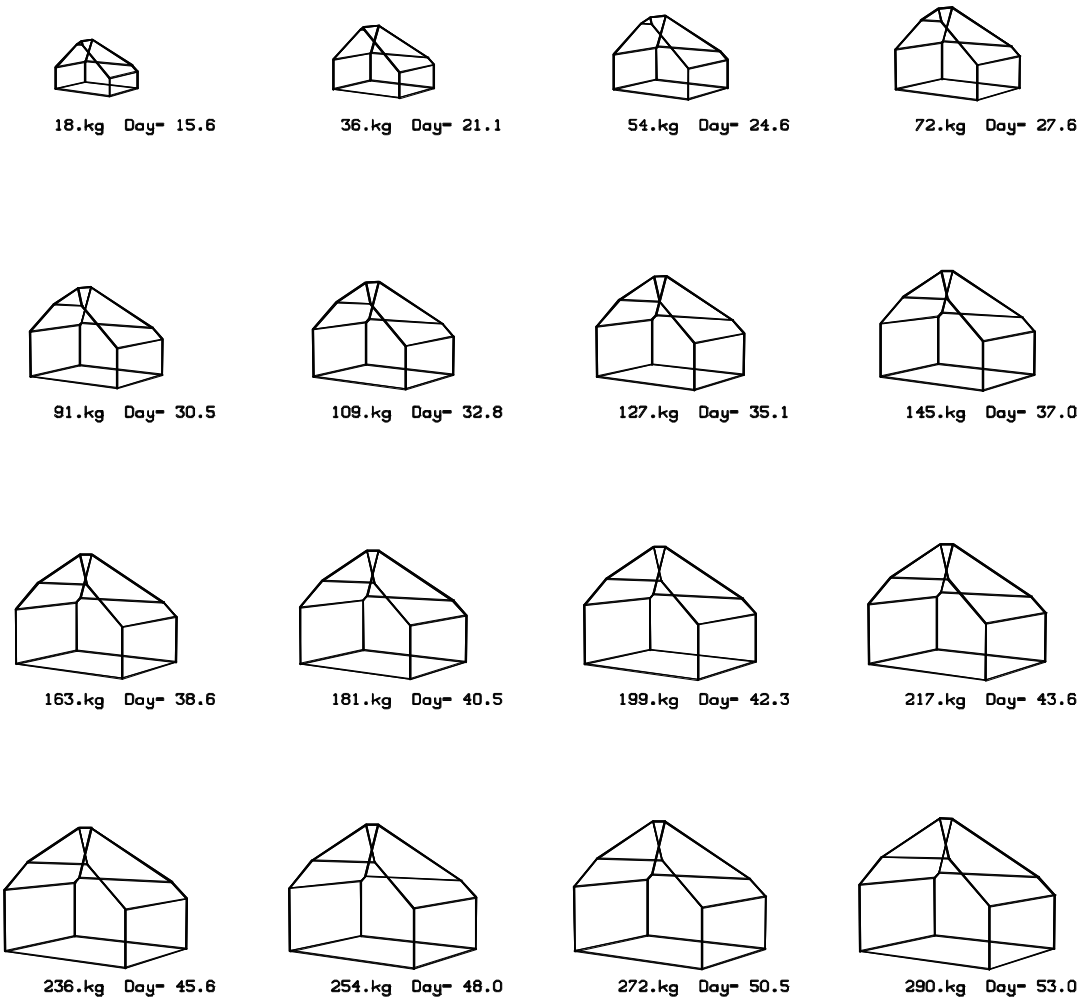

Figure 14. C-49 crystal shapes as a function of time (large anti-pyramid present on face 4, the back left face in this perspective, is not shown)

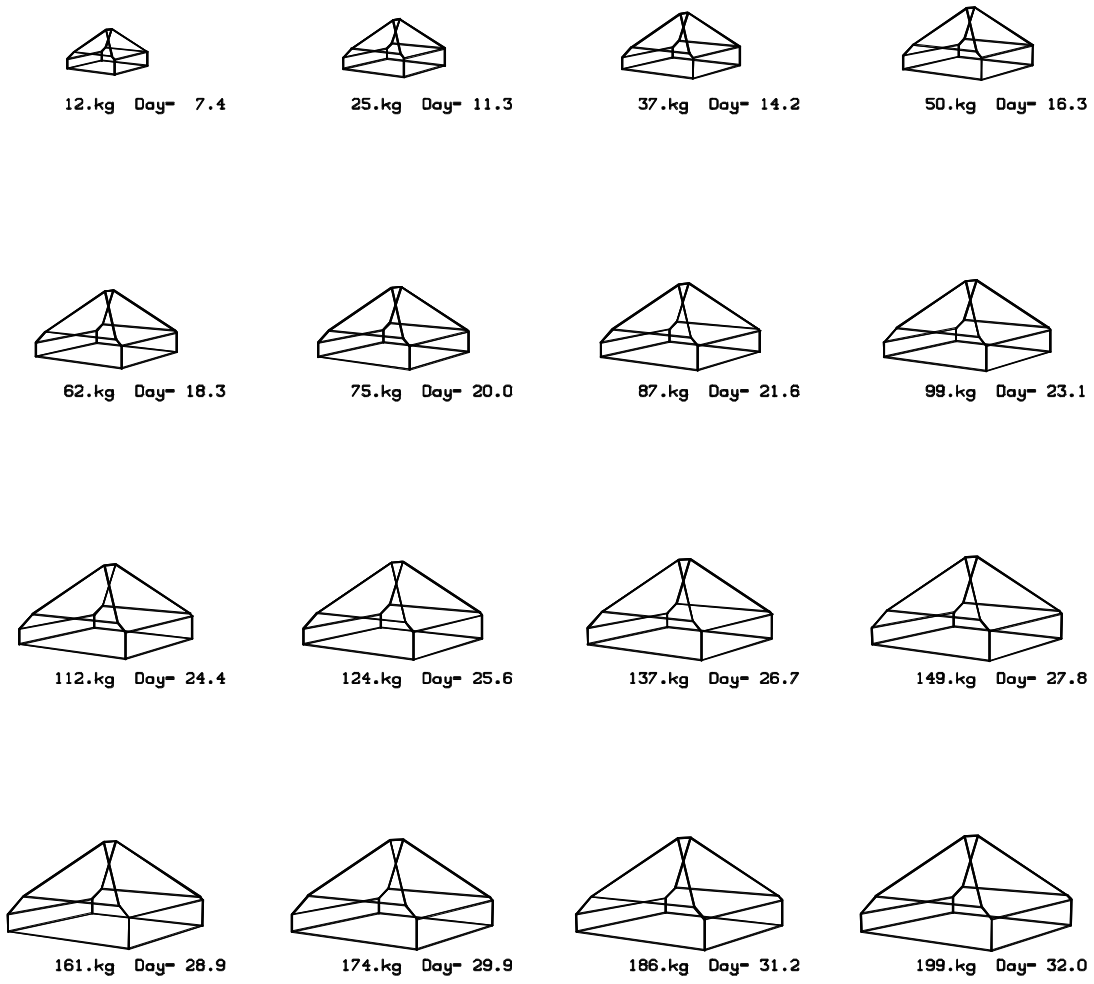

Figure 15. E-21 crystal shapes as a function of time

Note that the shape of these crystals did not evolve much during the growth period. It appears that the basic crystal shape was already established at the point the crystals were only 15kg. This shape was maintained over a nearly 20-fold increase in crystal mass. This suggests, barring early termination, that plate yield from a run could be estimated fairly early on, more on this later.

Crystal shapes from the 11 runs tend to fall into three groups:1) roughly symmetric; 2) one low or high prism face, and 3) two opposing high and low prism faces. The opposing high/low face crystals have significant C dimensions while those with only one unequal face tend to have small C values. The C dimension is that distance defining the top of the crystal. The division is about equal with crystals from runs B-15, C-47, F-21 and F-22 falling into group 1; B-17, F-21, C-48 and C-49 into group 2, and those from runs C-46, E-15 and E-17 in group 3. The final crystal shapes are shown if Fig. 16.

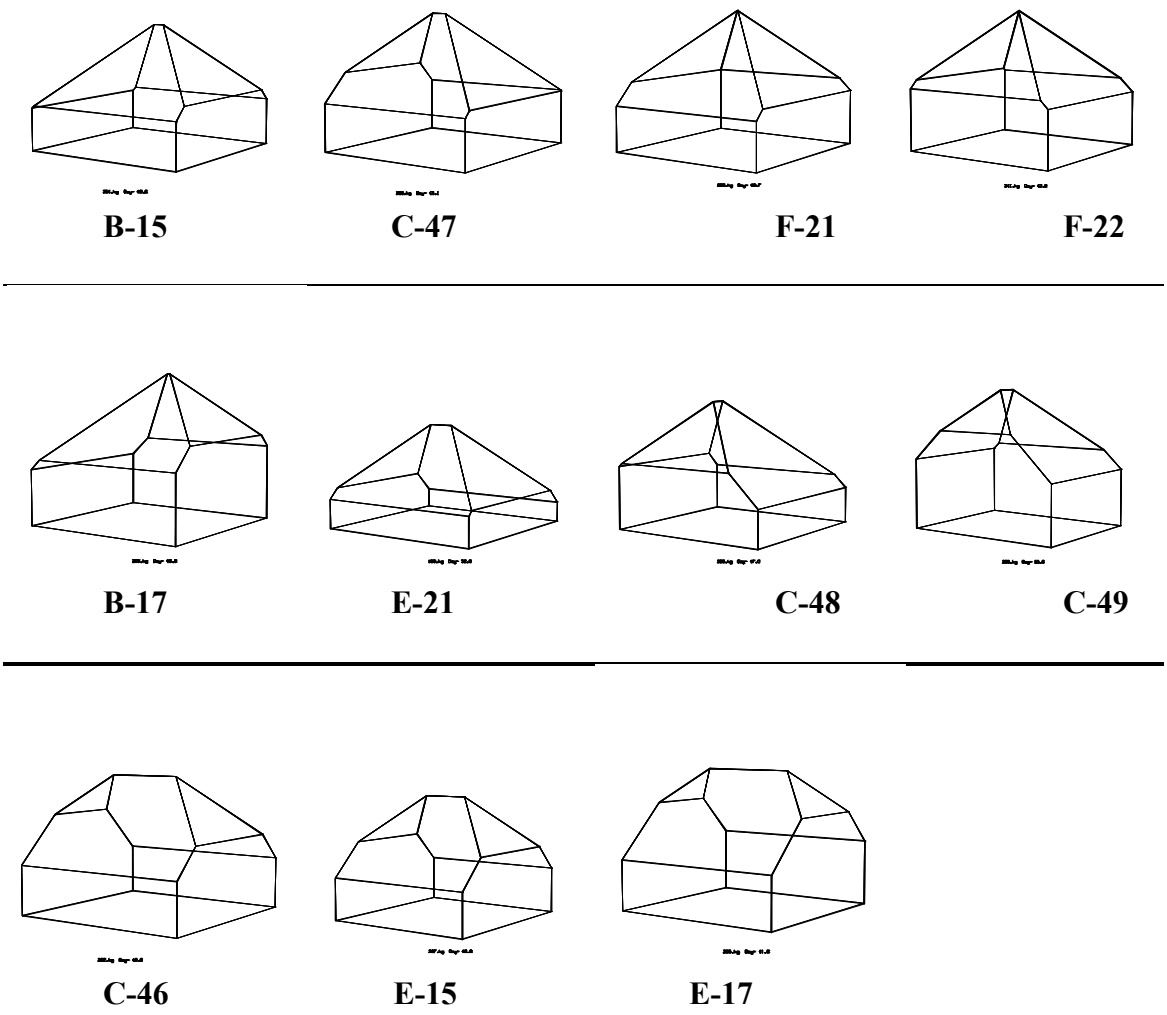

Figure 16. Final crystal geometries can be divided into three basic types. Crystals C-46 and E-15 have been included here, although only final prism heights are available for these two crystals. (The large anit-pyramid on the back left face of C-49 is not shown.)

Prism Locations and Heights: During a run the data on the lateral position of each prism face is recorded nearly everyday as is overall crystal height and approximate C-dimension. Heights of the prism faces are recorded less frequently, 1-3 times a week; however, they still form a fairly continuous record. The prism faces are numbered sequentially as shown in Fig. 17. In Figs.18-26 the prism location and height data, for the nine runs in which prism height data were recorded, are plotted. For completeness the prism location data are shown for the other two runs in Fig. 27.

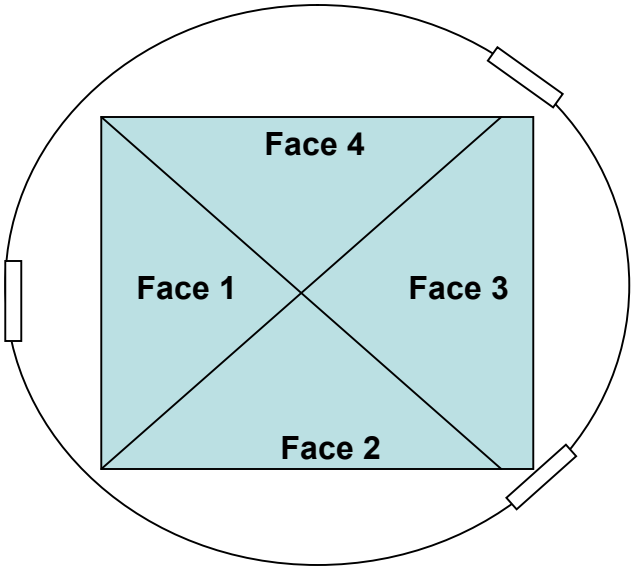

Figure 17. Face numbering scheme. This view is looking down on a crystal sitting on a platform. The small rectangular figures on the platform perimeter represent the position of the fins connecting the platform bottom to its top.

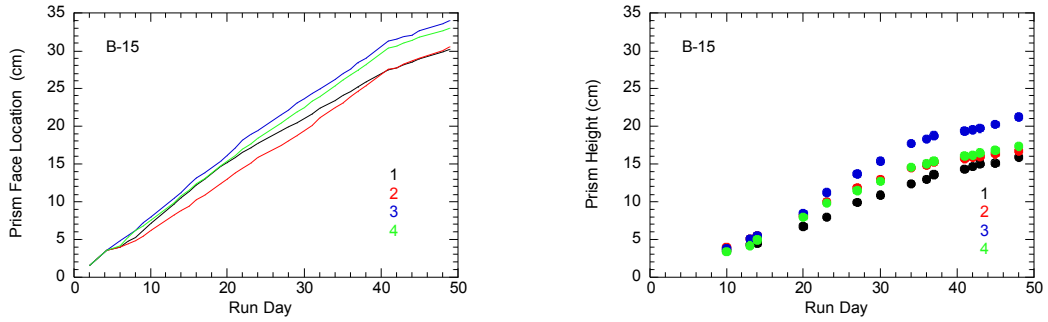

Figure 18. B-15 location (from the center of the seed) and height of each prism face.

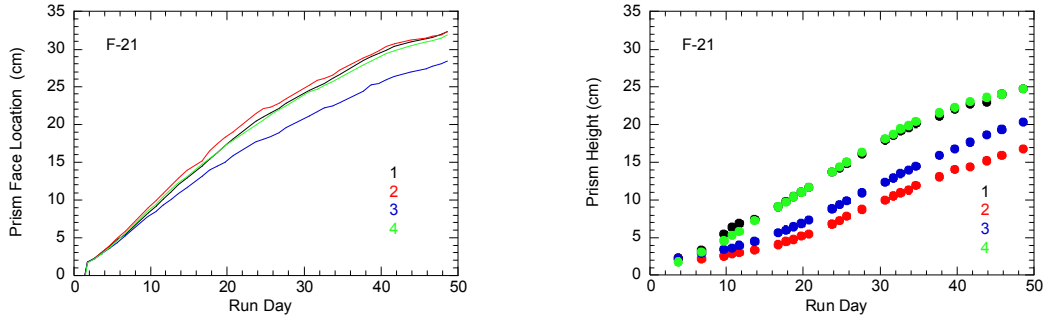

Figure 19. F-21 location (from the center of the seed) and height of each prism face.

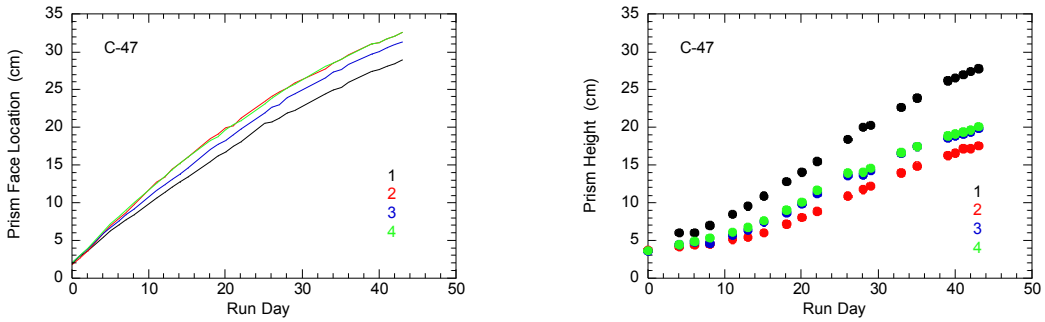

Figure 20. C-47 location (from the center of the seed) and height of each prism face.

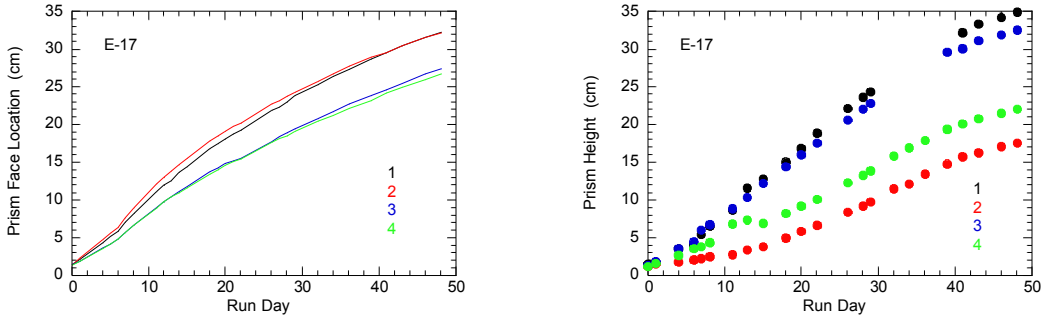

Figure 21. E-17 location (from the center of the seed) and height of each

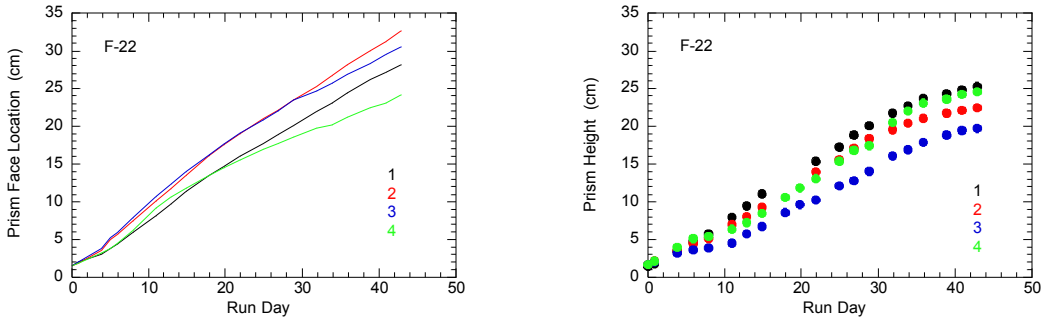

Figure 22. F-22 location (from the center of the seed) and height of each prism face.

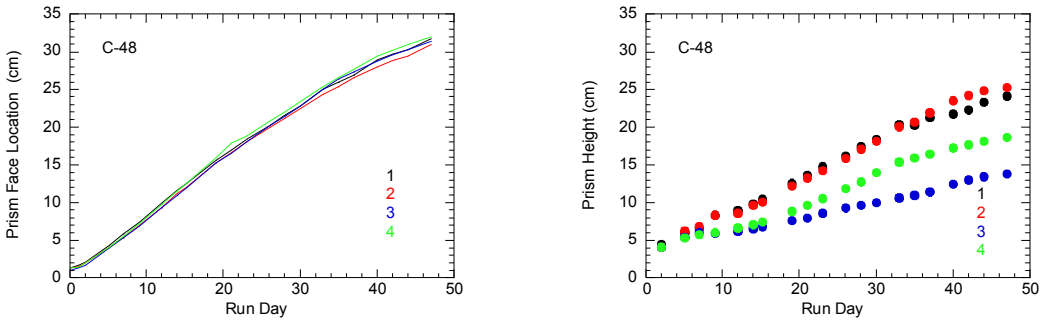

Figure 23. C-48 location (from the center of the seed) and height of each prism face.

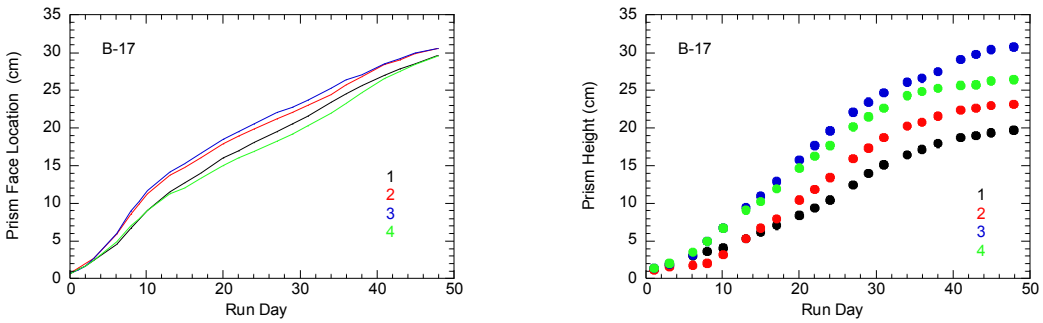

Figure 24. B-17 location (from the center of the seed) and height of each prism face.

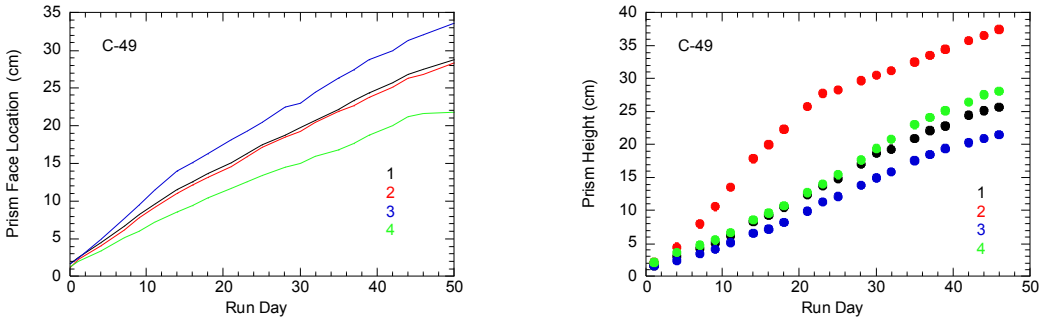

Figure 25. C-49 location (from the center of the seed) and height of each prism face.

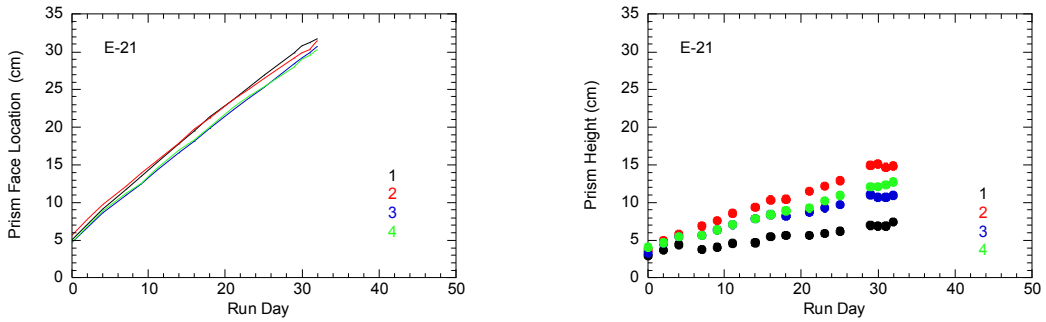

Figure 26. E-21 location (from the center of the seed) and height of each prism face.

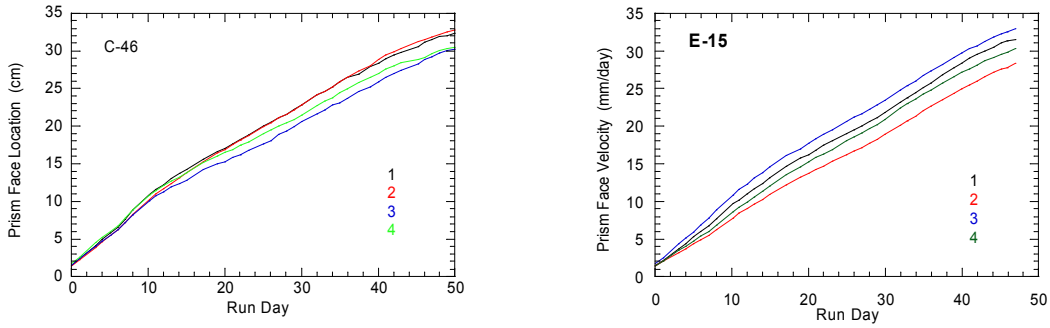

Figure 27. Prism-face locations for runs C-46 and E-15.

Prism- and Pyramid-Face Velocities: For the 9 runs with both prism height and location information face velocities for all eight major faces can be computed. These are shown in Figs. 28-36. Again for completeness prism face velocities are given for the other two runs in Fig. 37. It seems that the prism face velocities are more tightly bunched than the pyramid-face velocities. Part of the greater spread in the pyramid-face velocities may be a result of the fact that to compute them both prism-location and prism-height data must be use. The prism-face velocities, on the other hand, only require the use of the face location data.

Note that for run C-49 there was a large jump in its face-2 pyramid velocity around day 21. This jump was coincident with the size of the face-2 pyramid going essentially to zero. This was a result of its large velocity. We believe that the growth center causing the large growth was destroyed as the area went to zero. A new more modest growth center then began to control the face-2 pyramid velocity and consequently its velocity was greatly reduced. In fact, it appears that this new controlling growth center was smaller than those on any of the other faces. This is consistent with the generation of an essentially new pyramid face with few dislocations.

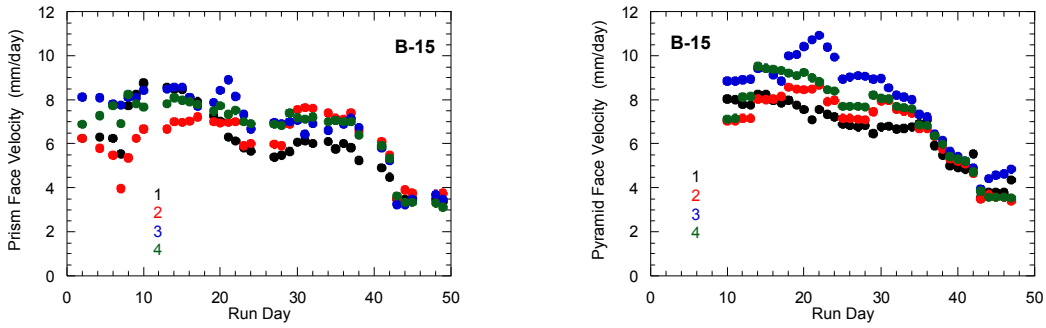

Figure 28. Prism- and pyramid-face velocities for run B-15.

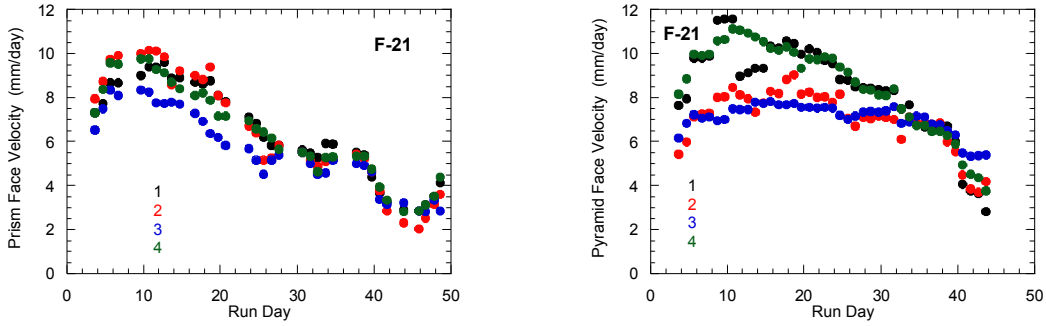

Figure 29. Prism- and pyramid-face velocities for run F-21.

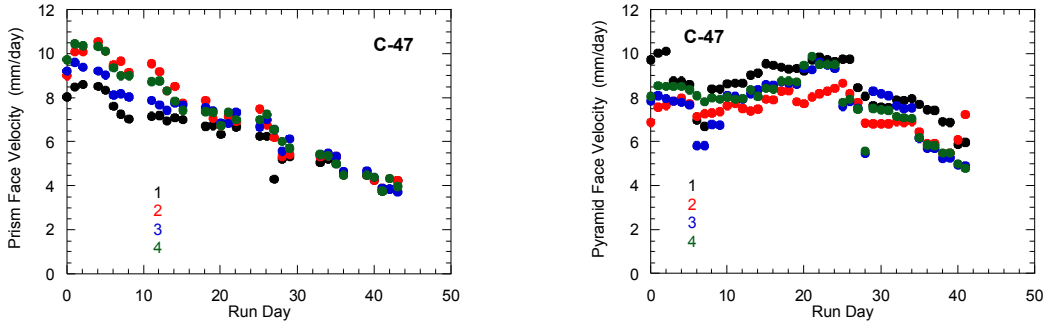

Figure 30. Prism- and pyramid-face velocities for run C-47.

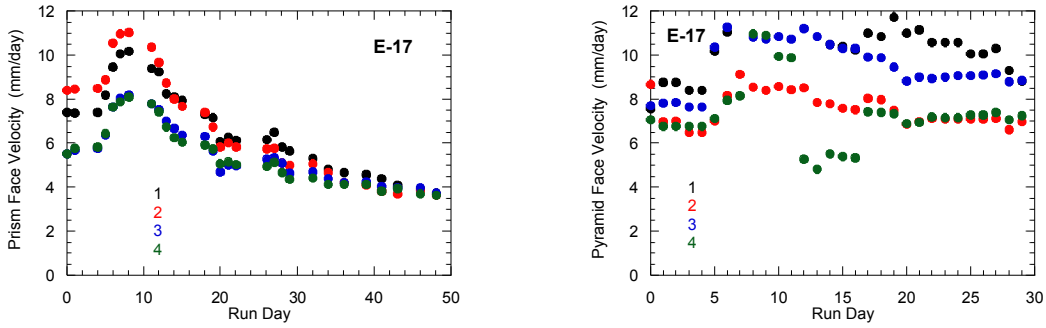

Figure 31. Prism- and pyramid-face velocities for run E-17.

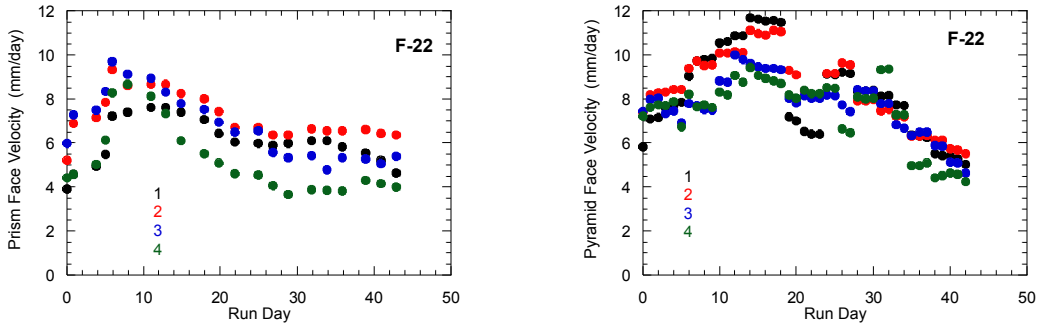

Figure 32. Prism- and pyramid-face velocities for run F-22.

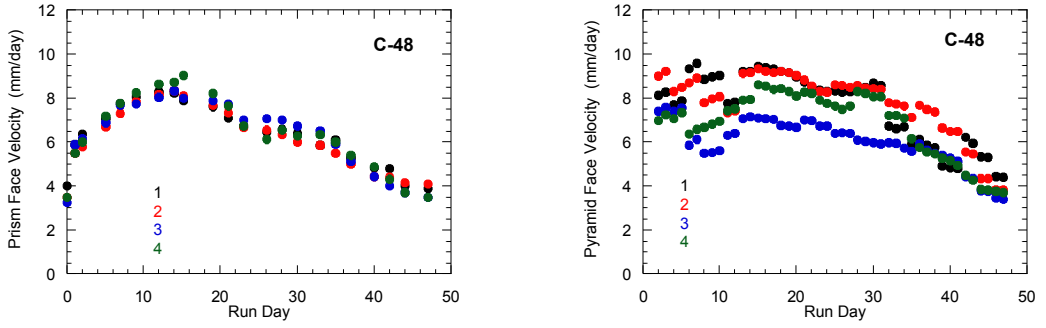

Figure 33. Prism- and pyramid-face velocities for run C-48.

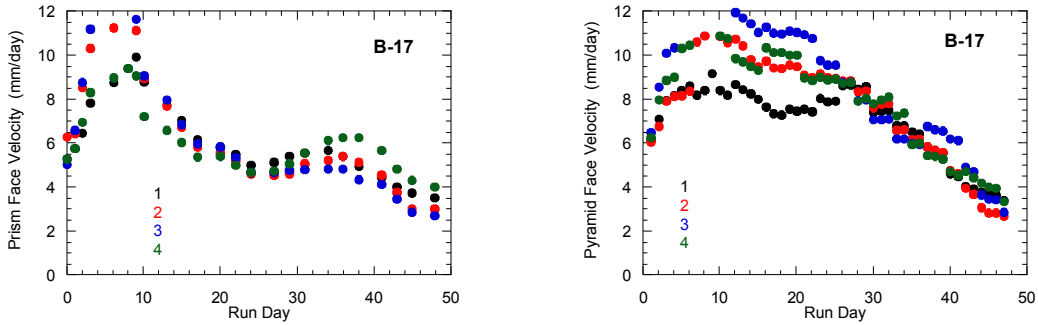

Figure 34. Prism- and pyramid-face velocities for run B-17.

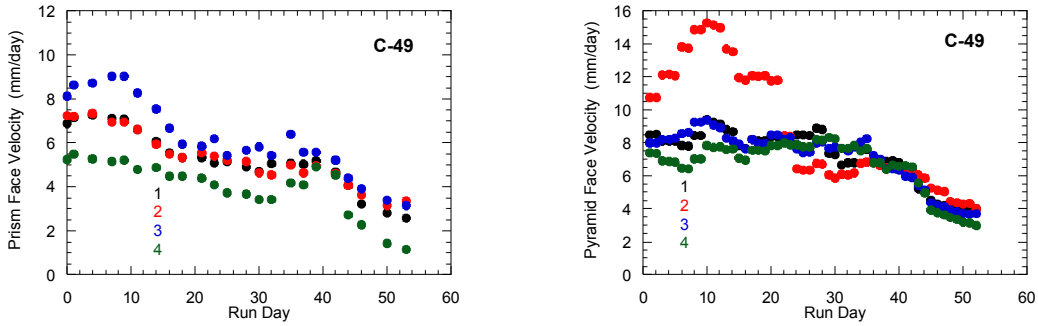

Figure 35. Prism- and pyramid-face velocities for run C-49.

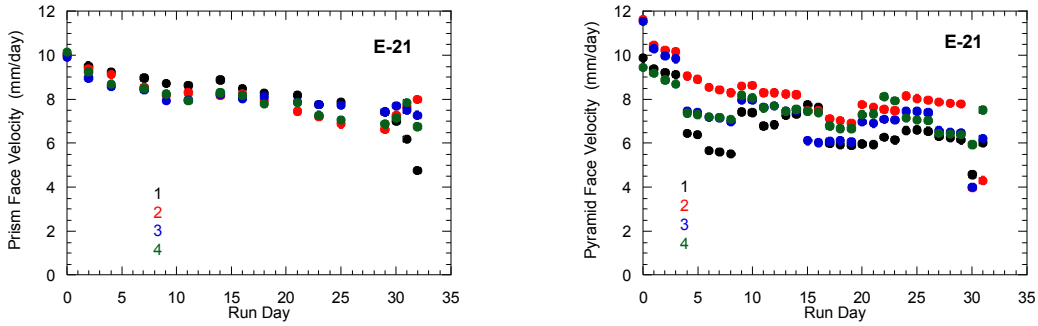

Figure 36. Prism- and pyramid-face velocities for run E-21.

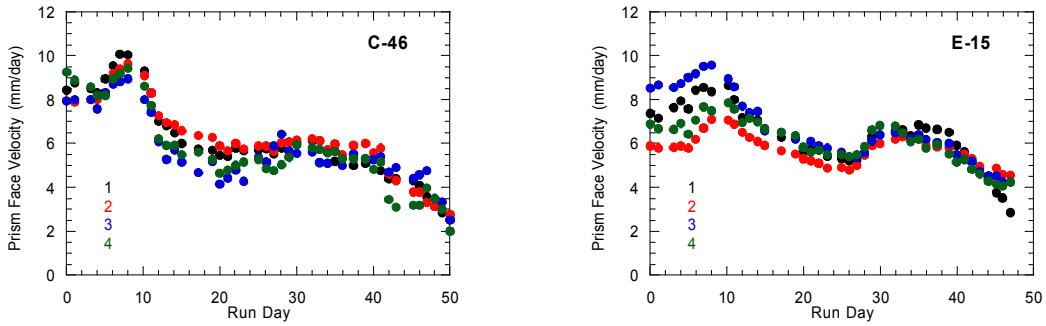

Figure 37. Prism-face velocities for runs C-46 and E-15.

ANALYSIS AND MODELING

The geometric data indicates that the shape of a crystal, in general, does not change significantly after the first few days of growth. If this is the case then we should be able to make useful prediction on ultimate plate yields fairly early in a run. In the following we first quantify the degree of invariability of crystal shape. We then look at relative face growth rates and show that growth rates of faces tend to maintain their relative size during a run. We suggest a means of predicting crystal growth based on early data and a growth model. We test this method using the data in hand. Finally, we demonstrate that seemingly minor variations in face velocity can produce the variety of crystal shapes and companion plate yields we see in our production boules.

Relative Prism-Face Heights and Positions

As already noted the evolving crystals preserve a remarkably constant habit. The degree to which the shape is invariant in time can be examined by looking at the relative heights and position of the crystal faces. To do this we have generated plots that show the ratio of these dimensions to average values at each point in time. A totally invariant shape would generate plots of these ratios with time that are flat. Computed relative face height and positions for the 9 runs in which prism heights were measured are shown in Figs. 38-41.

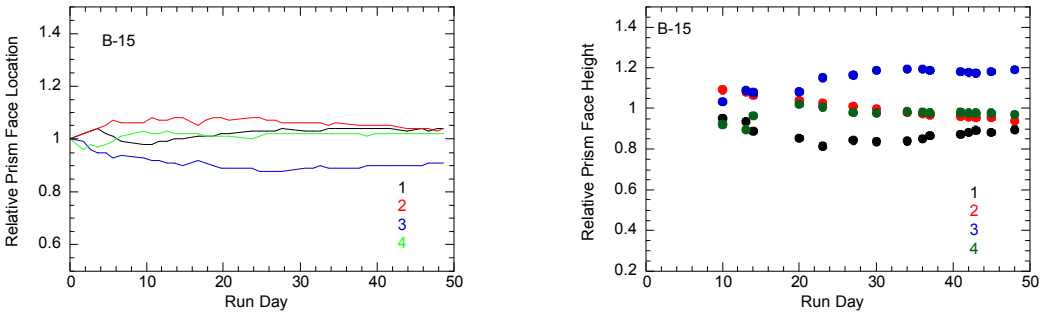

Figure 38. Relative prism-face locations and heights for run B-15.

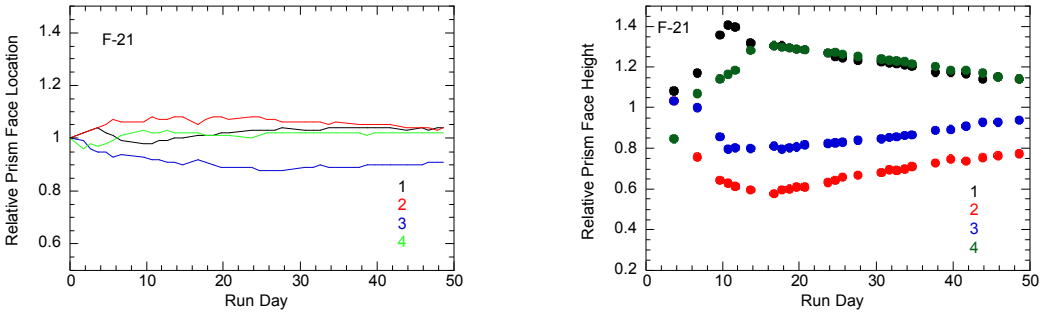

Figure 39. Relative prism-face locations and heights for run F-21.

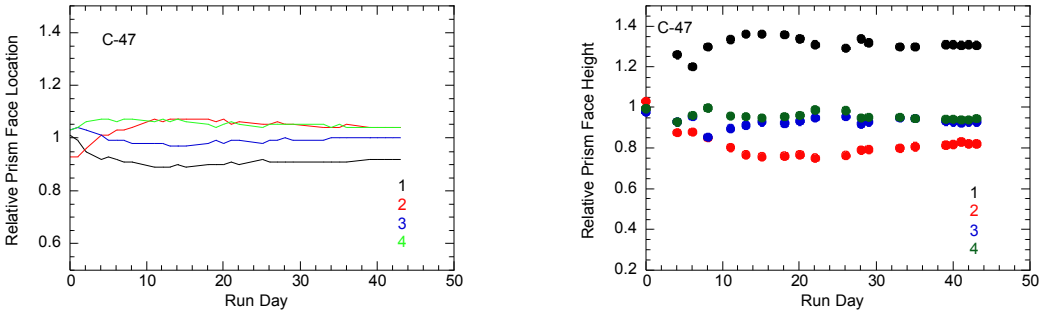

Figure 40. Relative prism-face locations and heights for run C-47.

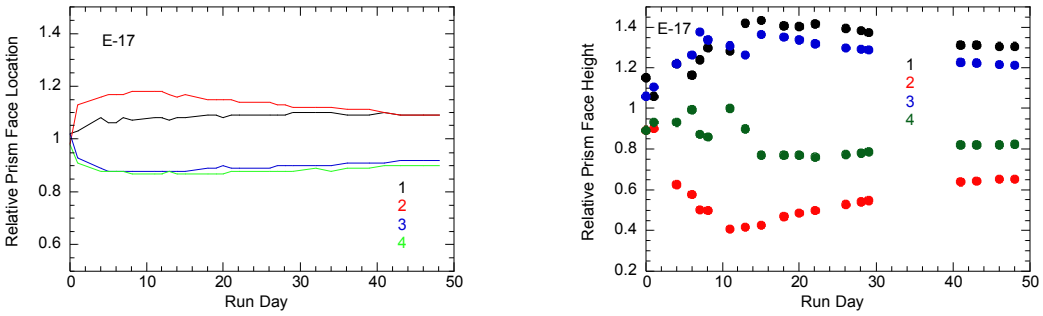

Figure 41. Relative prism-face locations and heights for run E-17.

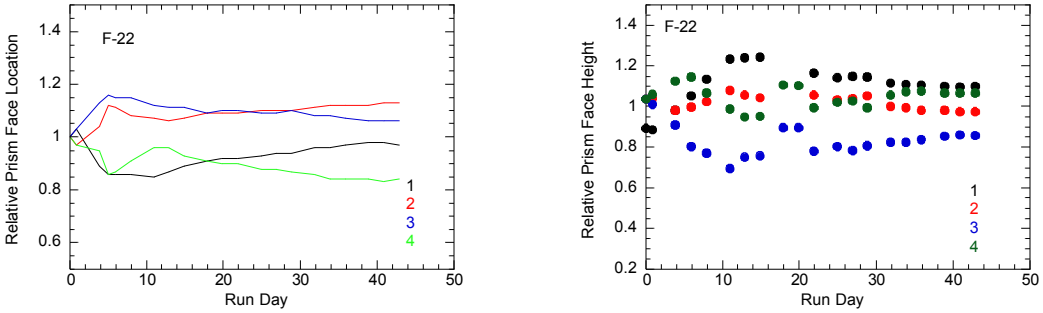

Figure 42. Relative prism-face locations and heights for run F-22.

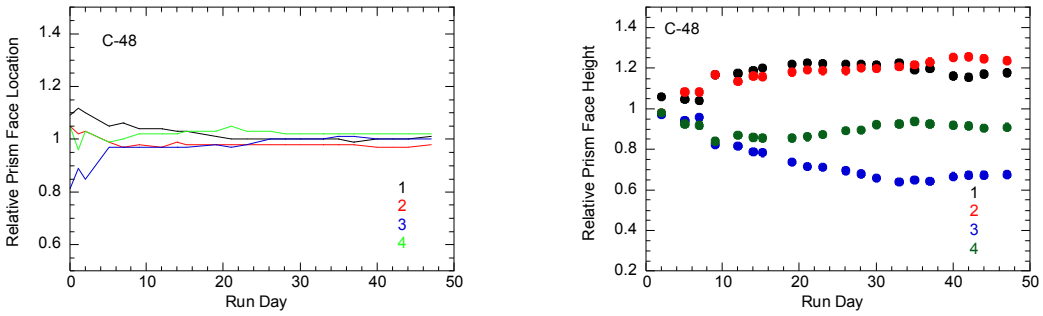

Figure 43. Relative prism-face locations and heights for run C-48.

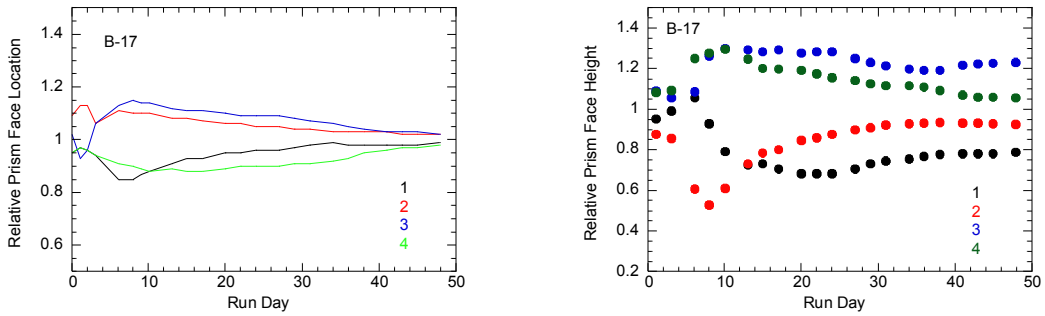

Figure 44. Relative prism-face locations and-heights for run B-17.

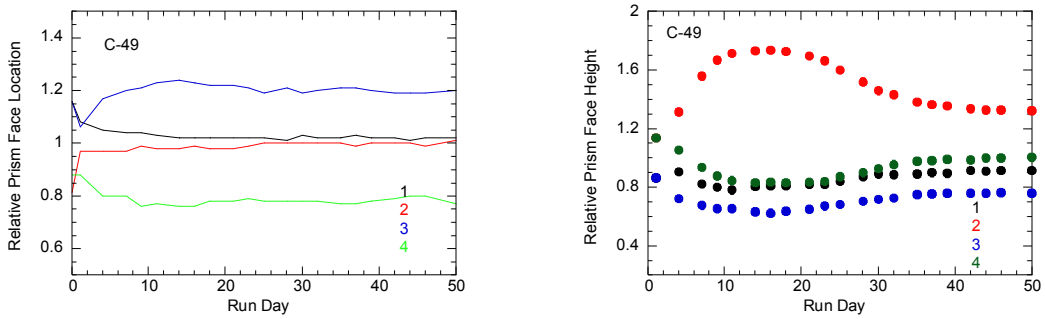

Figure 45. Relative prism-face locations and heights for run C-49.

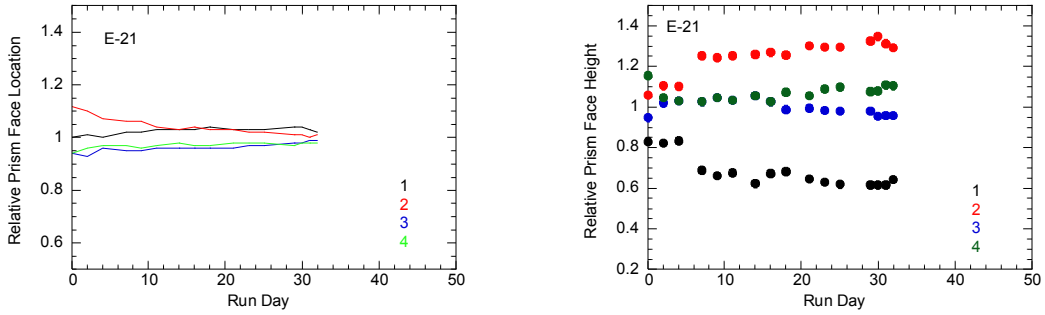

Figure 46. Relative prism-face locations and heights for run E-21.

Examining these figures we see that for the most part there appears to be an initial equilibration period in which ratios change. During this period the shape of the crystal is transitioning from its initial shape dictated by the seed geometry to a shape that is compatible with the face velocities that are present in that particular run. We can estimate this transition time by looking at the time it would take an idealized crystal to transform from its initial aspect ratio to its final stable aspect ratio dictated by face velocities. Using an average face velocity for both prism and pyramid faces of 6 mm/day and an initial crystal size of 2 cm then a transition to 90% of the final aspect ratio would take nine days. This is on the order of the transition times we see.

For the most part the position ratios are fairly constant after the equilibration period. There are exceptions to this general behavior. In at least two runs a long-term tendency for ratios to move toward each other is evident. In run B-17 the prism face locations move toward each other and in run F-21 a similar trend is seen but this time in the prism heights. We have no hypothesis as to why these two exhibit this behavior.

In run C-49 there is a substantial swing in relative prism height of face 2. This is a result of the jump in pyramid face velocity caused by the near disappearance of the face-2 pyramid.

Looking at the ratios from all the runs it is apparent that on average the spread in relative face heights is larger than the spread in relative face positions. The average variation between maximum or minimum ratios and one is about 0.1 for the prism location and more like 0.2 for the prism heights. This larger variability in heights could be caused by several factors. First, it may be that there is a greater variability in pyramid-face velocities than there is in the prism-face velocities. Looking back at the face velocity data there is some justification for this notion, but it is not overwhelmingly obvious. More likely it is a result of the fact that unlike the prism position, the prism height is a function of both a face's prism and pyramid velocities. Thus, one would expect the variability in prism height to be the sum of the variability in prism- and pyramid-face velocities. We believe this is the explanation for the greater prism height variability seen in Figs. 38-41.

Relative Prism-Face Heights and Positions

What drives the relative prism position and heights is the relative velocities of the various faces. The relative prism and face velocities for each run in which face growth data are available are shown as a function of time in Figs. 47-55. In each figure the velocities are shown relative to the average of all four faces. Unlike the relative position measurements there is no fundamental geometric reason that there should be a set transition period at the beginning of a run; and for the most part no easily identifiable initial transition is seen in the data.

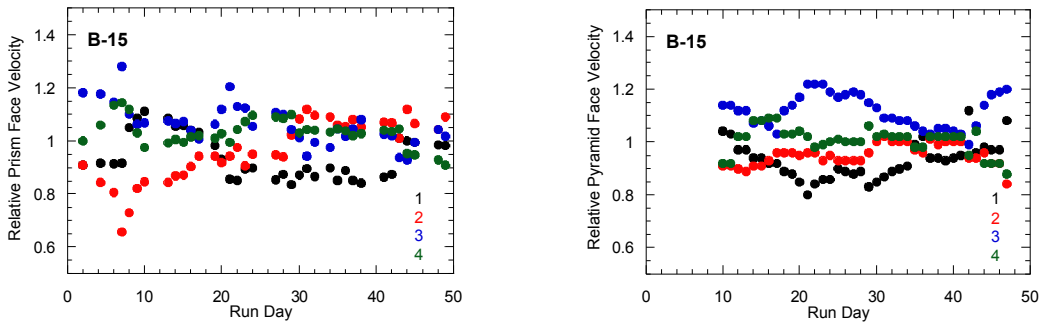

Figure 47. Relative prism- and pyramid-face velocities for run B-15.

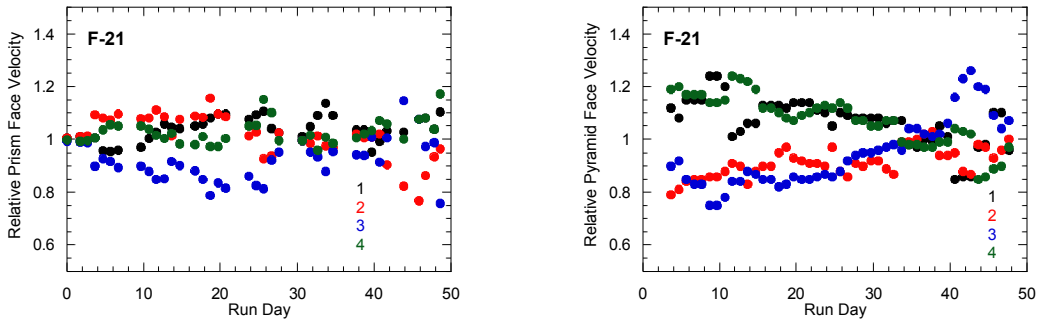

Figure 48. Relative prism- and pyramid-face velocities for run F-21.

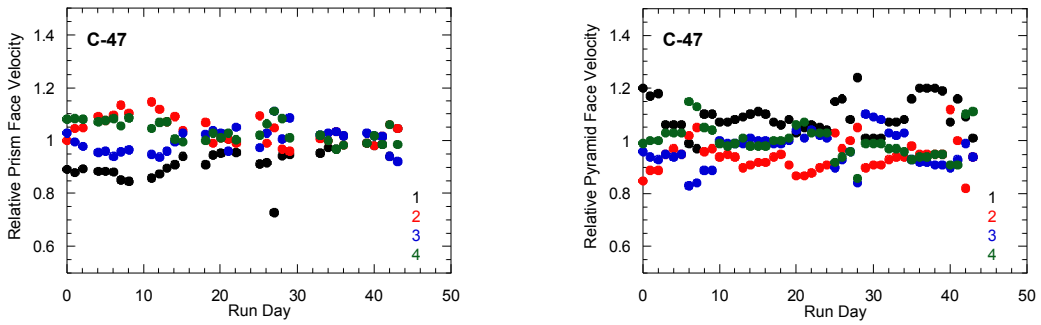

Figure 49. Relative prism- and pyramid-face velocities for run C-47.

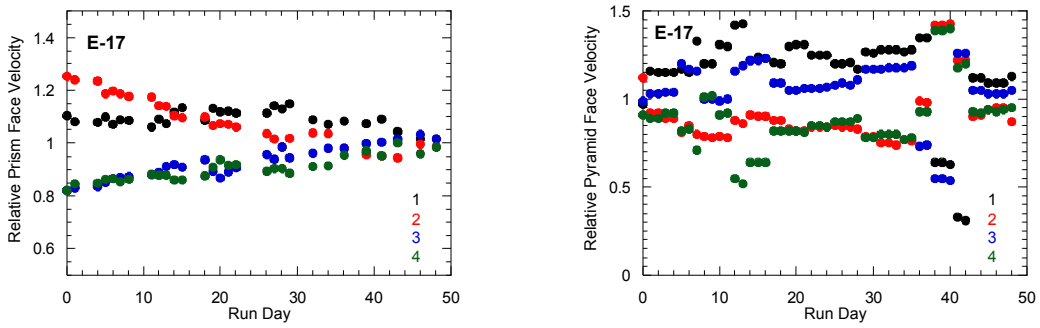

Figure 50. Relative prism- and pyramid-face velocities for run E-17.

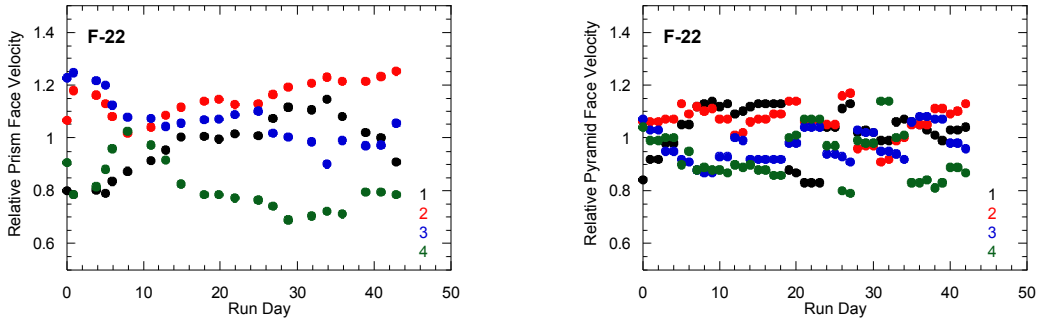

Figure 51. Relative prism- and pyramid-face velocities for run F-22.

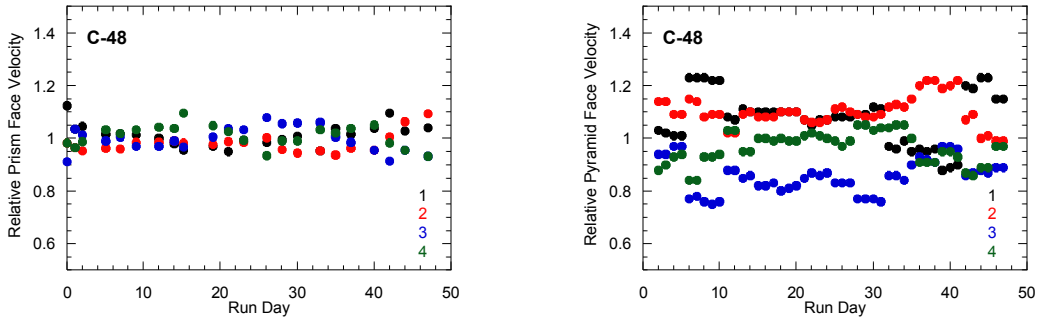

Figure 52. Relative prism- and pyramid-face velocities for run C-48.

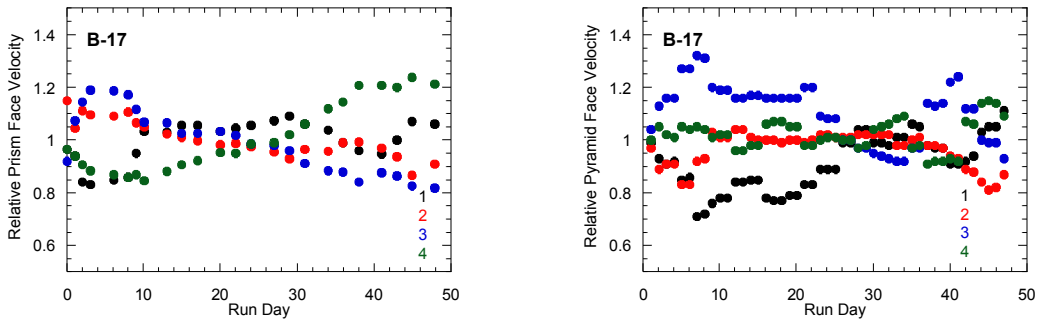

Figure 53. Relative prism- and pyramid-face velocities for run B-17.

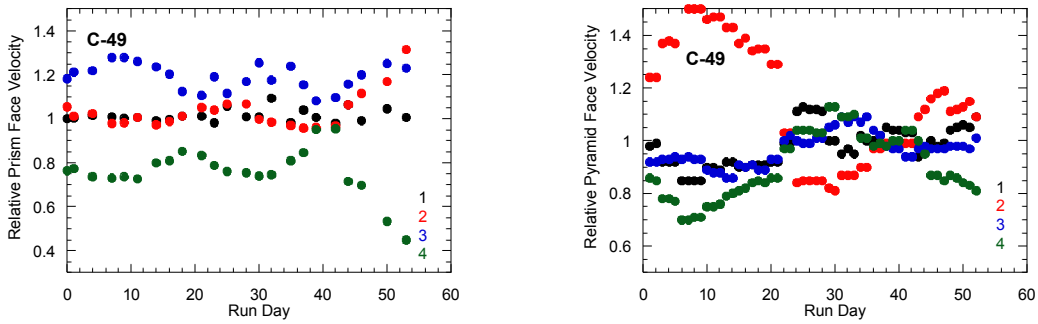

Figure 54. Relative prism- and pyramid-face velocities for run C-49.

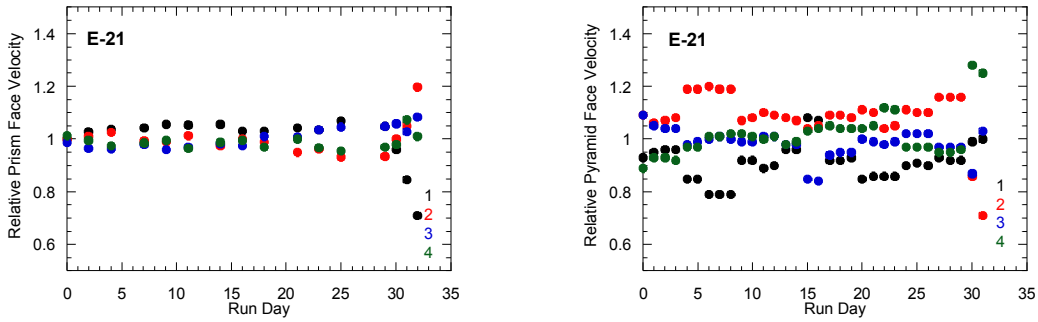

Figure 55. Relative prism- and pyramid-face velocities for run E-21.

Even though face velocities change by factors of two to three during a run the velocity ratios tend to change on average by only about 10-20%. In two runs, E-21 and C-48, the prism-velocity ratios are all very near one and invariant in time. In other runs differences in relative face velocities are apparent and in most cases the differences persist throughout the run.

In most runs there is some change in velocity ratios with time; however, no consistent trends are obvious. The largest variation is present in C-49 pyramid face-2 velocity. This is related, as described previously, to the near disappearance of the pyramid face on side 2. As suggested by the prism height and position data, run E-17 showed consistent long term trends in relative prism velocities and F-21 in pyramid velocities.

Since all sides of a crystal are exposed to the same ambient supersaturation levels the variability in relative face velocities seen in Figs. 47-55 cannot be attributed to errors in temperature or solution concentration. Errors from measurement uncertainty are only a few percent for prism location and height. Thus velocities computed from data are also probably accurate to a few percent. The prism velocities are more accurate than the pyramid velocities for reasons described previously. Thus the roughly 40% difference between the lowest and highest face velocities often present in the data reflect real differences in how those faces are responding to a given supersaturation level. Whether this difference is attributable to difference in dislocation strength, and/or mass transfer limitations is not evident from the data.

Plate Yield

The number of optical plates that can be cut from a boule is, especially for doubler plates, a complicated function of size and shape of the boule. This fact motivates our interest in determining how well final crystal shape can be predicted for a given production run. Final crystal shape is a result of the integration of all eight crystal face velocities over the course of a production run. From the above we can see a good-news/bad-news story line. The bad news is that crystals grown under similar conditions produce crystals with variations in relative growth rates of their faces. At this point we have no way of predicting this variability. Thus predicting the details of the final boule geometry is impossible. On the good-news side the data seem to indicate that the relative growth rates of faces, at least when comparing prism faces to prism faces and pyramid faces to pyramid faces, remain roughly constant during a run. This manifests itself in the striking similarity in shapes between 5-10 day old crystals and shapes after 40-50 days of growth. Thus, it would seem by examining growth rates early on one could make reasonable estimates of final crystal shape and plate yields. In the following we attempt to quantitatively examine this assertion.

Theoretical yields of NIF doubler plates (14 mm blanks, 11mm finished) are shown in Fig. 56-60 for the nine crystals examined in this memo for which both time varying prism location and height data are available. All but one of these crystals yielded doubler plates. These crystals will be used as a database against which to check any proposed predictive scheme.

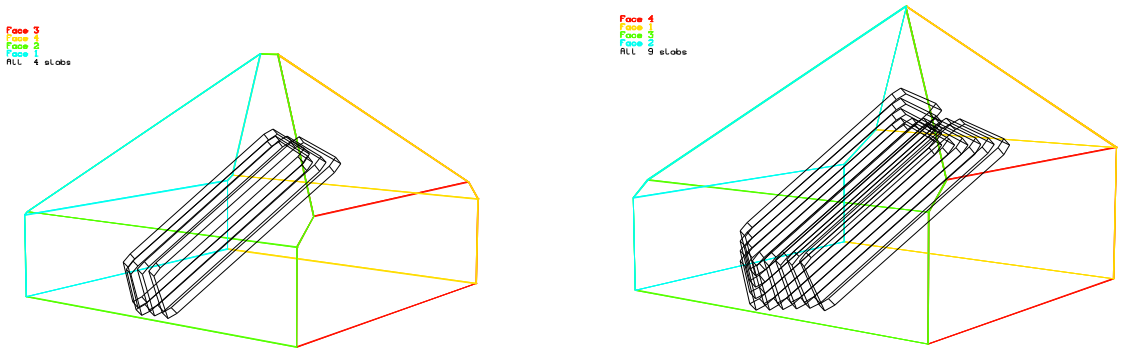

B-15 **F-21**

Figure 56. Final crystal and theoretical doubler-plate yields for runs B-15 and F-21.

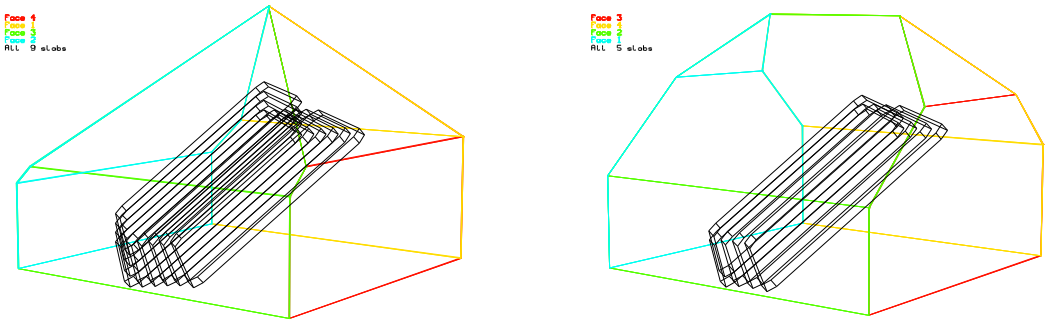

C-47 **E-17**

Figure 57. Final crystal and theoretical doubler-plate yields for runs C-47 and E-17.

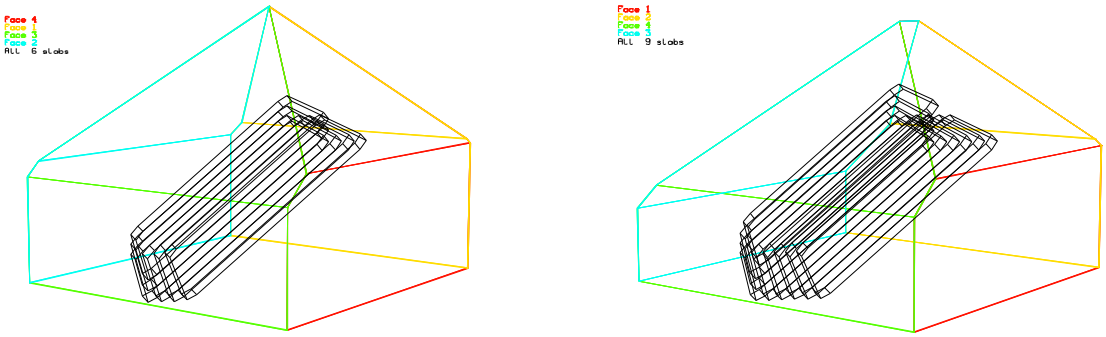

F-22 **C-48**

Figure 58. Final crystal and theroetical doubler-plate yields for runs F-22 and C-48.

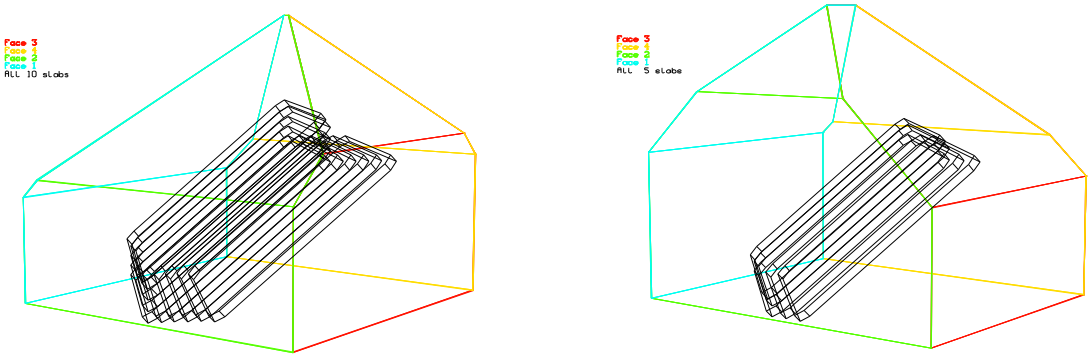

B-17 **C-49**

Figure 59. Final crystal and theoretical doubler-plate yields for runs B-17 and C-49.

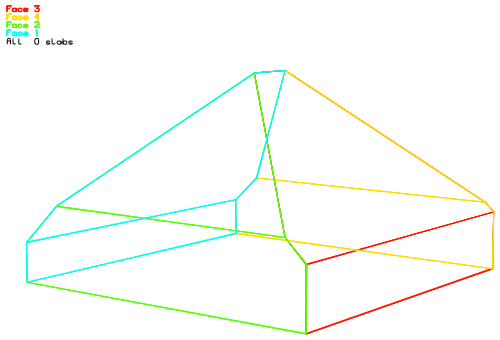

E-21

Figure 60. Final crystal and theoretical doubler-plate (14 mm blanks, 11 mm finished) yields for run E-21.

The simplest predictive scheme would simply use the approximate invariance of relative prism heights and positions. The problem with this approach is that it is critical to know the ultimate aspect ratio of a crystal along with relative prism heights and positions. The aspect ratio is a function of the relative growth of the prism and pyramid faces. The results presented above have not established that this is a constant. In fact, we know from historical data that the aspect ratio tends to vary throughout the run and thus it is difficult to predict based on early growth results.

An alternate approach is suggested by our previous success in using a simple kinetic based model to match the evolving average height and width of a crystal. This model assumes that face velocities can be computed using the following expressions:

$$R_{m/s} = \frac{A}{\rho_{solid}} \exp\left(\frac{-E_a}{RT}\right)\left(\rho_{KDP} - \rho^*_{KDP}\right)^2, \tag{1}$$

$$v_{face} = \left(1 - \frac{[Al]_{crystal}}{30\,ppm}\right) R_{m/s}, \tag{2}$$

and

$$[Al]_{crystal} = K[Al]_{solution}, \tag{3}$$

where $E_a = 47$kJ, $A = 26$ m^4/kg-KDP ·s and ρ_{solid}=2335 kg/m^3 (density of KDP crystal). The driving force uses the difference between solution KDP levels and saturated conditions in kg/m^3 units. The aluminum distribution coefficient was obtained from a limited data set and is assumed to be temperature dependent and given by the line shown in Fig. 61.

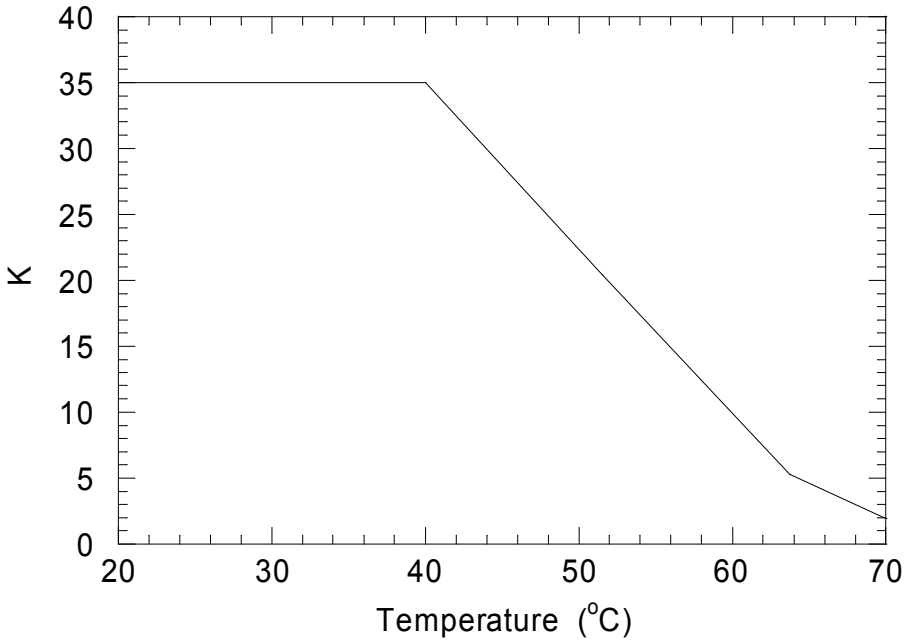

Figure 61. Equilibrium distribution coefficient used in the modeling.

In the previous work a single value was used for A. We modify this approach for use here by assuming that there is a different A for each face. The value of the As is established by using data from a production run at some point in time. From the data we can obtain values for $R_{m/s}$ for each face, T, ρ_{KDP}, ρ^*_{KDP}, and $[Al]_{solution}$; therefore, we can compute As for each face. Based on these values, the use of Eqs. (1-3), and appropriate material balances the geometric evolution of a crystal can be computed.

For each of the nine runs As were computed. In computing these values the following equilibrium relation for KDP in water (historically used in run spreadsheets) was used
$\text{kg - KDP/kg\_Solution} = 0.1165 + \left(3.002x10^{-3}\right)T_C + \left(8.577x10^{-6}\right)T_C^2$.
Values were computed at several times during the initial portion of the run. The target times chosen were 10, 15 and 20 days. Insufficient data was available to use earlier times. The computed As and the run day used to compute them are listed in Table 2. The values shown were then used to compute the evolution of a crystal throughout the remainder of a run. These calculations were done using measured temperatures. From these calculations average relative errors in values for final prism heights (h) and prism positions (x) were computed where the relative error is defined as

$$Error = 100\sum_{i=1}^{4}\frac{(x_i - y_i)}{4\bar{y}}.$$

Here x_i and y_i are the computed and measured prism height or position respectively for each face. These errors are one measure of how well growth behavior can be computed from early growth data using the model given in Eqs. (1-3).

Table 2 indicates that the computed errors in prism position are lower than those for prism heights. The location errors average about 5% and the height errors about 15%. This is probably mostly a function of the fact that the height is dependent on both prism- and pyramid-face velocities while the prism location is only a function of prism-face velocities. Interestingly, there seems to be no consistent trend for the errors to be reduced as later time data is employed. This suggests that the simple model used does not capture all the physics. Recent work has suggested that mass transfer plays a significant role in setting face velocities. In the simple model used here it is assumed to play no role.

Table 2. Values of the face growth parameter A for each of the eight faces computed at several experimental times. Also shown is the relative error in final crystal prism heights (h) and positions (x) computed using the model and these As.

		Prism As (m^4/kg s)				Pyramid As (m^4/kg s)				Errors(%)	
Run	Day	1	2	3	4	1	2	3	4	x	h
B-15	14	32	25	32	30	27	27	33	33	7	13
	20	27	26	31	29	29	32	40	34	8	25
F-21	10	42	25	21	24	29	20	17	27	4	25
	14	26	26	22	25	25	21	21	29	1	14
	20	30	31	22	27	35	30	26	34	5	12
C-47	11	27	35	30	33	32	27	29	29	5	6
	15	26	30	28	28	34	29	31	31	5	14
	20	27	28	29	29	38	32	38	39	8	25
E-17	11	25	27	20	20	35	20	26	23	5	14
	15	27	26	22	21	34	25	35	17	5	14
	20	30	28	23	24	50	31	40	31	3	15
F-22	11	21	24	25	23	28	27	24	22	9	17
	15	20	23	22	18	27	27	25	24	6	10
	20	22	25	23	17	28	31	24	25	5	11
C-48	9	30	29	29	30	35	31	20	25	1	22
	15	29	29	29	32	33	32	25	29	3	15
	21	33	33	35	35	38	37	30	35	3	19
B-17	10	15	16	16	13	13	17	20	17	8	12
	15	27	27	28	23	29	34	40	33	5	9
	20	24	22	23	21	27	34	39	35	8	30
C-49	8	25	33	28	31	29	25	22	27	5	11
	18	26	30	28	28	34	29	31	31	5	14
	20	27	28	29	29	38	32	38	39	8	25
E-21	9	45	42	41	42	38	44	41	41	1	12
	14	39	37	36	36	34	38	33	33	1	7
	21	36	33	35	34	26	33	30	32	2	4

The computed As run from a low of 13 to a high of 45 m^4/kg-KDP ·s. In some cases, run F-22 for example, the As computed at each time are fairly consistent; however, in most cases this in not true. It is also clear that in a given run the computed As for the four faces can show a considerable range. There is little doubt that this variability is real since errors in measuring velocities are relatively low, especially for prism faces, and the most error-prone variable, supersaturation, is not an issue for comparisons at an instant in time in a single run.

As part of the extrapolation calculations, final doubler-plate yields were computed for extrapolations made from 10, 15 and 20-day data. These are shown in Table 3. The computed plate yields are compared to the yields computed from the final measured boule dimensions. For the most part the estimates are in good agreement with the values obtained from final measured dimensions. With a single exception, the estimates made using the 20-day data are within one or two plates of the actual values. The exception is C-49 where the computed yields are much larger. This discrepancy is a result of the large jump taken by one of the C-49 pyramid-face velocities on day 20. Calculations made based on data taken before day 20 can not reflect this drastic step change in velocity.

Table 3. Doubler-plate yield data compared to estimates from extrapolations based on three different run times. Here the projections use the time/temperature of actual run to extrapolate to a final crystal geometry.

Run	Data	Based on Day		
		20	**15**	**10**
B-15	**4**	3	3	-
F-21	**9**	9	8	10
C-47	**8**	9	8	8
E-17	**5**	5	0	7
F-22	**6**	6	5	7
C-48	**9**	11	11	11
B-17	**10**	9	9	10
C-49	**5**	10	8	9
E-21	**0**	0	0	0

Estimates of plate yields presented in Table 3 assume that the projected run will continue to the same end point temperature as the actual run. In a real run of course the final temperature will not be known and the end point for extrapolation must be set by some other means. A full-term run is terminated for one of several reasons: 1) the temperature reaches ~16^{o}C ; 2) the crystal gets too wide to be removed from the platform or hits one of the vertical platform fins; or 3) the crystal grows over the edge of the platform. Thus in an ongoing run if one wants to estimate final plate yield one of these criteria will determine the end time for an extrapolation. We have recomputed plate yields using these criteria for terminating the run rather than the actual run time. Specifically we used the following termination criteria: 1) temperature reaches 16^{o}C; 2) one of the crystal corners grows 1 cm beyond the edge of the nominal 90 cm platform; and 3) the crystal width in the limiting direction (Y-direction) exceeds 64 cm. The results of these calculations are shown in Table 4. Notice that the plate-yield estimates are poorer than those made previously. The average error in plate yield is 2 plates for extrapolations based on data up to 15 and 20 days and 3 plates for those based on 10-day data. A maximum error of 5 plates is made for all three extrapolation base times. While still useful, it is clear that better extrapolation procedures would be helpful to more accurately predict the final plate yield from early data.

Table 4. Doubler-plate yield data compared to estimates from extrapolations based on three different run times. Here the projections were terminated when the projected crystal was 1-cm over the platform or it became too wide.

Run	Data	Based on Day		
		20	**15**	**10**
B-15	**4**	5	5	-
F-21	**9**	10	8	5
C-47	**8**	3	11	11
E-17	**5**	6	0	0
F-22	**6**	9	8	10
C-48	**9**	12	12	11
B-17	**10**	10	10	8
C-49	**5**	10	0	0
E-21	**0**	0	0	0

Face Growth Parameter *A*

To determine how prism- and pyramid-face growth parameters on average differ, we have computed average (4 faces) values of prism and pyramid *A*s. We have chosen to use the 15-day data from Table 2. The averages are shown in Table 5. Also shown in the table are system temperature, average crystal width, crystal mass, growth solution aluminum levels (as ratios to KDP), and EDTA concentrations. A number of observations can be made based on the data in the table. First, the average *A* for the prism and pyramid faces are nearly equal. Second, the run in which no aluminum was present show the highest average prism *A* value. This later behavior is expected based on the established influence of aluminum on prism-face velocity. The average pyramid *A* value, 30 m^4/kg-KDP ·s, is consistent with values computed from recent kinetic measurements at 68°C. The pyramid *A*s from the kinetic experiments averages 37 with a range of 30-60 m^4/kg-KDP ·s. However, the *A*s for the prism faces are all higher than the average *A* value, 20 m^4/kg-KDP ·s, obtained from kinetic measurements. Many are even larger than the upper end of the 10-30 m^4/kg-KDP ·s range found in the kinetic measurements.

Table 5. Average growth parameters for prism and pyramid faces along with other system properties at a nominal time of 15 days into the run.

					Average As (m^4/kg s)			Al	EDTA
Run	Day	T(C)	W(cm)	Mass(kg)	Prism	Pyramid	A Ratio	ppm	Mol%
B-15	14	72	21	9	29.8	30.0	1.0	1	0.014
F-21	14	73	25	13	24.8	24.0	1.0	1.1	0.016
C-47	15	73	30	36	28.0	31.3	1.1	0.9	0.014
E-17	15	72	27	19	32.8	27.6	0.8	1.1	0.019
F-22	15	72	25	20	20.8	25.8	1.2	1.6	0.022
C-48	15	72	24	17	29.8	29.8	1.0	1.3	0.021
B-17	15	70	27	22	26.3	34.0	1.3	1.4	0
C-49	18	71	27	27	28.0	31.3	1.1	0.8	0.019
E-21	14	71	35	35	37.0	34.5	0.9	0	0
Ave.					28.6	29.8	1.1		

This prism result is very disconcerting since it implies that the kinetics measured on small crystals can not be applied to large boules. This conclusion is only tentative at this point since there are several factors that could change our opinion. First, the analysis done here assumes a squared dependence on supersaturation. The kinetic data suggests a lower power. This fact along with the recently demonstrated importance of mass transfer in boule growth clouds the direct comparison of large boule data and kinetic measurements. Second, it may be that we have not seen the true distribution of kinetic rates from the small crystals. This is important since in the large boules a number of growth centers are present and the one that leads to the highest net growth rate is the one that determines movement of a face.

The behavior of A values with solution aluminum levels is further explored in Fig. 62. A values for both prism and pyramid faces obtained from data at day 15 are plotted as a function of growth-solution aluminum levels (Al/KDP). As anticipated there appears to be no trend of pyramid face A values with aluminum levels. On the other hand, there is an indication that the prism As do decrease with increasing aluminum levels. This trend is largely seen in the two extreme values: A=37 m^4/kg-KDP ·s at 0 ppm Al, and A=21 m^4/kg-KDP ·s at 1.6ppm Al. It is a little surprising that the aluminum influence shows up at the high temperatures present on day 15 since aluminum levels in the forming crystal layer are more than an order of magnitude lower at 70°C than they are at lower growth temperatures.

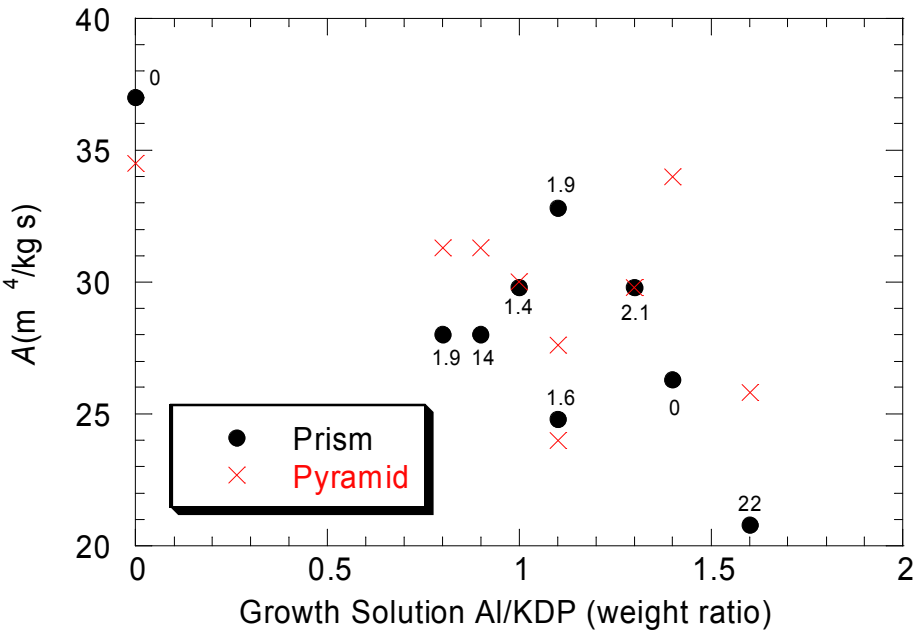

Figure 62. *A* values for prism and pyramid faces at 15 days as a function of solution aluminum content. The numbers by each prism data point are the EDTA levels in mol% x 100.

The *A* values shown in Table 2 clearly show the variability of *A* values obtained from the boule growth data. To quantify this variability we have computed standard deviations for the computed *A*s. In these calculations *A* values were computed for all nine runs at run times from 5 to 40 days. At each run time the data for all prism and pyramid faces were collected for use in computing standard deviations. These standard deviations as fractions of the mean are listed in Table 6. The computed standard deviation for the prism faces is very consistent for the times listed. The composite standard deviation for the prism faces expressed as a fraction of their mean values is 10%. The pyramid faces show more of a variation in standard deviation with run day, but still cluster near their composite value of 14%.

Table 6. Statistics of relative face growth for runs B-15, C-47, E-17, F-21, F-22, C-48, B-17, C-49 and E-21.

	***A* Standard Deviation/ Mean**	
Day	**Prism**	**Pyramid**
10	0.10	0.16
15	0.09	0.14
20	0.08	0.13
25	0.09	0.10
30	0.10	0.12
35	0.10	0.12
40	0.10	0.17
Combined	**0.10**	**0.14**

The distribution of *A*s about a mean is not highly skewed and is reasonably represented by a normal distribution. This can be seen by looking at the distribution of the ratio of prism- and pyramid-face velocities to their mean shown in Figs 63. These data are for velocities at 15 days. There is some skew toward a longer tail for ratios greater than one but it is not large.

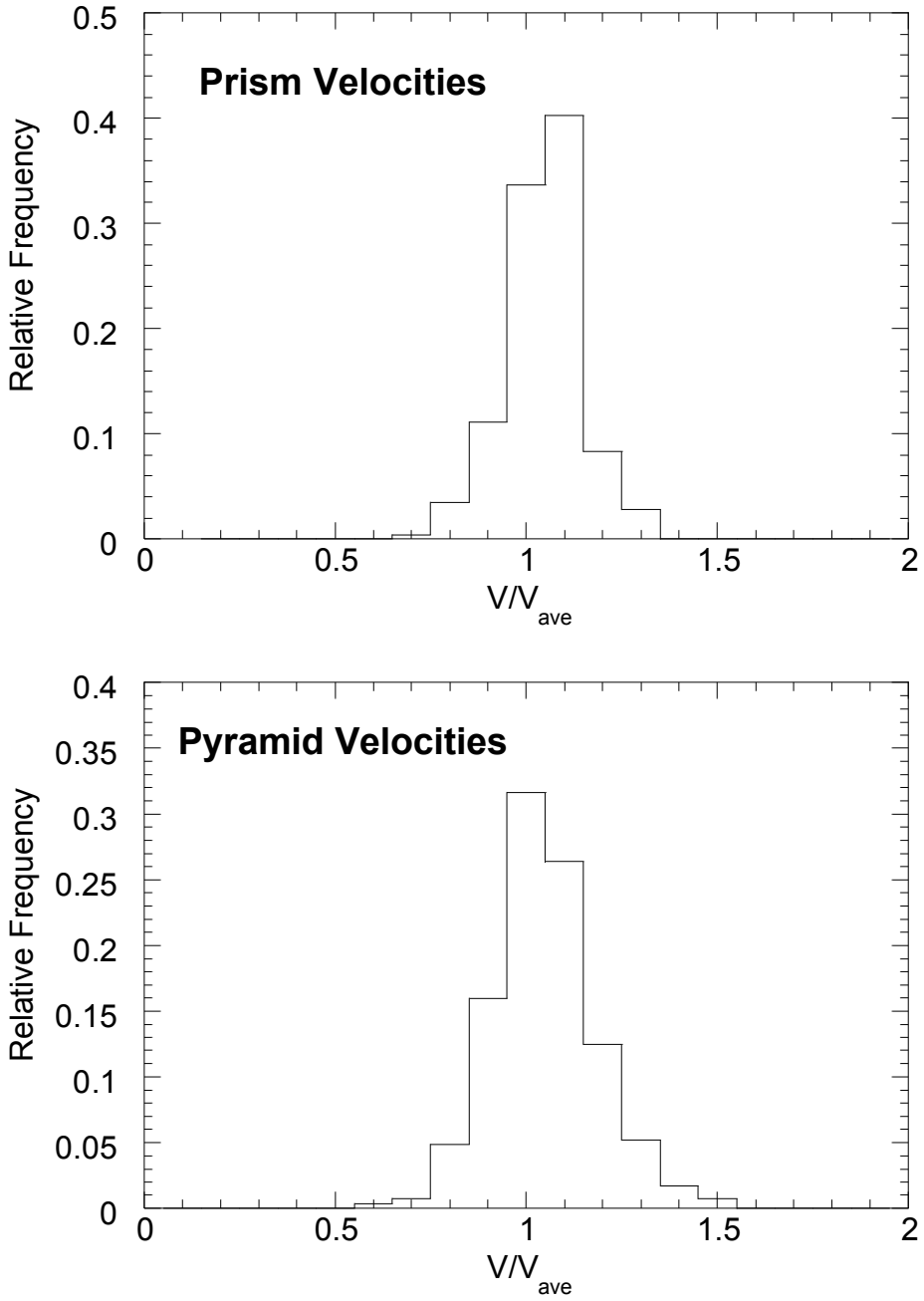

Figure 63. Frequency curves for prism- and pyramid-face velocities on run day 15.

It is of interest to demonstrate that the type of variation we have seen in *A* values can explain the type of variability in crystal geometry that we routinely see in our production runs. First, it is instructive to see what changes in assumed growth rates in one or two faces do to crystal shape. In Fig. 64 crystal shapes are shown in which we assume the prism and/or pyramid face of side 3 has a growth rate either 10% above or below the other faces. The figure demonstrates the fact that fast growing prism faces lead to low prism heights and vice-a-versa. Conversely, high pyramid rates lead to high prism face heights and low pyramid velocities to low heights. If both prism and pyramid face velocity change in the same direction it is hard to see the effect by casual observation of

crystal shape (3rd row of crystals in figure). On the other hand, if face velocities vary in opposite directions, the change in crystal geometry is marked (bottom row of crystals).

If instead of allowing only one face to have a different face velocity we assign relative face velocities in a random fashion to all faces, we obtain rather striking results. These results are shown in Fig. 65. The velocities were assigned using a normally distributed distribution of relative velocities with a standard deviation of 10%. This variability is somewhat less than that obtained from looking at *A* values obtained from run data. Still, the variation in the crystal shapes is very reminiscent of those of actual boules, Fig. 16. The simulated boules have aspect ratios of 0.65 to 0.93, while the boules in Fig. 16 have aspect ratios from 0.62-0.96. Note that in generating the face velocities the relative pyramid/prism velocity was set to 1.1 in order to give an ensemble average aspect ratio of 0.75. This is equivalent to running a system with a constant Al level. In the runs that generated the actual boules aluminum levels varied. Still, an assumed constant ratio of prism to pyramid velocities generates an aspect ratio range as large as the real boules that had the additional influence of variable aluminum levels. Clearly, one should be very cautious in using a small number of runs to draw conclusions about the influence of any parameter on aspect ratio.

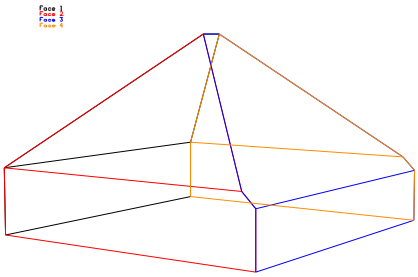

Side 3-Prism 110%

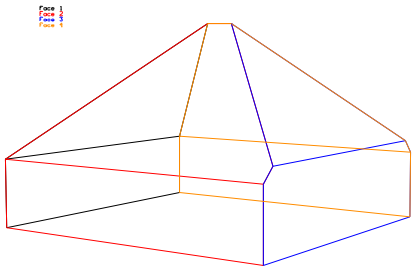

Side 3-Prism 90%

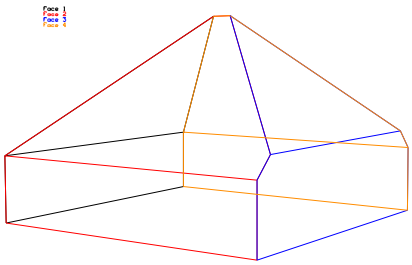

Side 3-Pyamid 110%

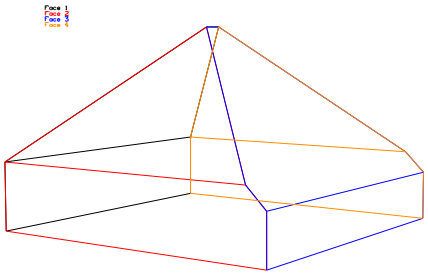

Side 3-Pyramid 90%

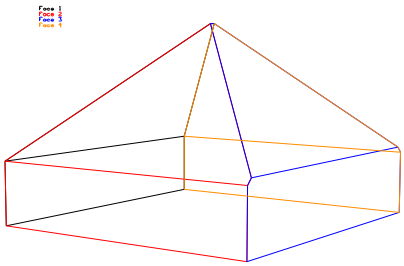

Side 3 Prism & Pyramid 90%

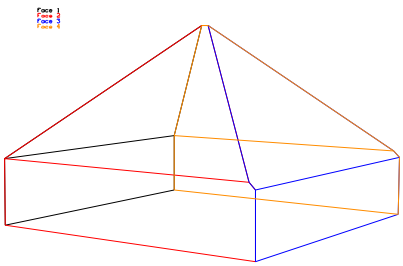

Side 3 Prism & Pyramid 110%

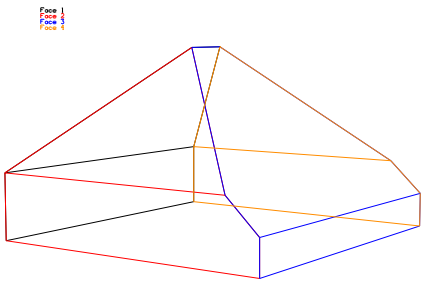

Side 3 110% Prism & 90% Pyramid

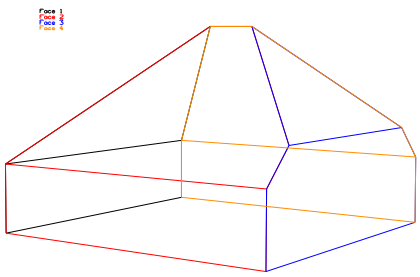

Side 3 90%Prism & 110% Pyramid

Figure 64. Crystal shapes generated by assuming ±10% difference in side 3 face growth rates.

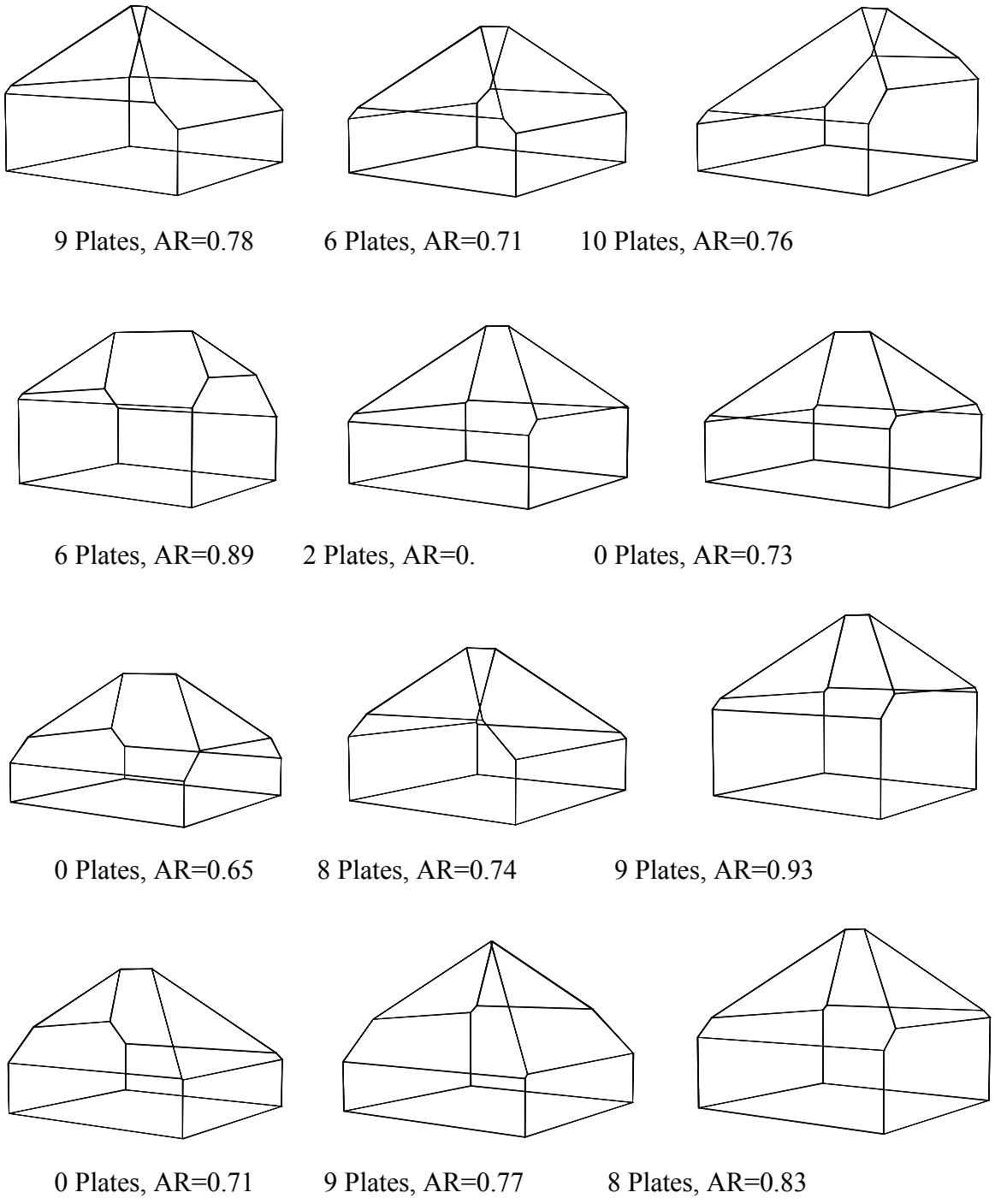

Figure 65. Crystal shapes generated by assigning velocities to each face using a relative face velocity that is normally distributed with a standard deviation of 10% relative to an average.

The theoretical yield of doubler plates was also computed for the crystals shown in Fig. 65. The basic crystal shapes do not depend on crystal size; however the plate yield does. So we limited the crystal size in the calculations in the same way they are limited in actual production runs. The limiting criteria included: mass, Y dimension, height and diagonal size. The diagonal size referred to here is that from the crystal center to crystal

corner and is important in determining when the crystal grows beyond its supporting platform. The computed plate yield for the crystals in the figure runs from 0-10 with an average of 5.6 and a standard deviation of 4. Interestingly this average plate yield is very close to that seen in the production boules. Again, this results points out the danger of drawing conclusions about improving plate yield by adjusting some operating variable on the basis of only a few runs. Here, only the observed, and assumed to be random, variation in relative face velocities generates crystals with a large range of yields.

The crystals shown in Fig. 65 are just 12 realizations of the assumed normally distributed random variation of face velocities. As such, they need not display the average characteristics of a large collection of realizations. We have computed standard deviations of a number of measures of crystal geometry using a large number (1000) of randomly generated crystals. We found the following standard deviations (as a percentage of average values):

- Total crystal height – 9%
- Aspect ratio – 8%
- Base symmetry (X/Y) – 10%
- Prism heights – 25%

These are based on a standard deviation of face velocities of 10% for both prism and pyramid faces. Note the large variation in prism height by the interaction of prism and pyramid velocities.

Extrapolated Results and Data

In this subsection we use the extrapolation method outlined previously to compute the important system parameters. In these calculations an early calibration time, generally about 15 days, was chosen to obtain the required prism and pyramid-face A factors; using these, and the experimentally measured temperatures, the growth of the crystal from the calibration time to the end of the run was computed. Here we compare computed results for each run to the actual data.

The results are presented below as a series of 12 plots for each run. In the plots solid lines show the computed results while circles and crosses show results obtained directly from measured data. The plots are self explanatory with a few exceptions. The plot titled "Prism Aluminum" is the computed level of aluminum in the prism-face material, no line is shown for the pyramid since these levels are assumed to be very low. The plot labeled "k Values" is a plot of average linear-growth parameters for the prism and pyramid faces. The averaged linear growth-parameter is defined by

$$\overline{v_{face}}\rho_{solid} = k\left(\rho_{KDP} - \rho^{*}_{KDP}\right)$$

and is closely related to minimum average mass transfer and kinetic coefficients.

B-15 (Fig. 66): A calibration time of 15 days was used for this run. Two late aluminum additions were used during this run, their timing can be determined by examining the "Solution Aluminum" plot. The projected face velocities do a fair job in following the

actual velocities. There is an upward trend in the face-3 pyramid velocity near day 20. This is not captured by the calculations. This is not surprising since the simple model has no mechanism for differentiating the performance of faces after the initial determination of *A* values. Also, the prism velocities beyond day 30 trend higher than the computed values suggesting, perhaps, that their temperature dependence is too high in the model. Finally, note that the computations do a fair job representing the aspect ratio, a critical parameter in determining plate yield.

F-21 (Fig. 67): A calibration time of 15 days was used for this run. Four late aluminum additions were used during this run. Again the projected velocities are in reasonably good agreement with the data. An exception is the face-3 prism velocity that shows a steeper drop after day 15 than calculated. Interestingly, the computed aspect ratio is essentially equal to the final measured value; however, the computed trend is not the measured trend.

C-47 (Fig. 68): A calibration time of 15 days was used for this run. Three late aluminum additions were used during this run. Notice that the computed prism velocities after day 34 drop well below the measured values. The drop in the computed velocities is a result of the high aluminum levels computed for the prism material during late times. This discrepancy suggests that the aluminum retardation factor is too large either because the simple correlation given by Eq. (2) and/or the aluminum segregation coefficient is too high at the lower temperatures.

E-17 (Fig. 69): In this case a calibration time of 20 days was used. A later time than the nominal 15 days was chosen because of the odd data associated with the face-4 prism height. On day 15 there is an abrupt flattening of the trend with time. Since it is possible that this is a problem with the data we chose to stay away from this time region. Two late aluminum additions were used during this run. Velocity trends are followed fairly closely with two major exceptions. There is a large apparent drop in face 1 and 3 pyramid velocities between day 30 and 40 not reproduced by the computed values. On closer examination however it looks like this may be an artifact of the large data gap in the side 1 and 3 prism heights during this time interval. Notice that after 40 days the agreement in computed and measured velocities is better. In this case the computed and measured trends in aspect ratio agree very well.

F-22 (Fig. 70): A calibration time of 15 days was used for this run. No late aluminum additions were used in this run. Computed velocities track the measured velocities fairly well except for the prism-face velocities between days 30 and 40. During this period all but one prism face has a velocity above the computed values. Again this behavior is driven in the model by the aluminum retardation factor since it is this time period in which the largest aluminum levels in the prism material are computed. In this run much of the aspect ratio trend is captured by the computations.

C-48 (Fig. 71): A calibration time of 15 days was used for this run. Three late aluminum additions were used in this run. This run had remarkably equal prism velocities. Again, we see that the predicted late prism velocities are low, driven by high computed aluminum levels in the crystal. During the time interval (days 35-45) when the computed prism velocities are low the computed pyramid velocities are high; however, not as high

as the prism velocities are low. The aspect ratio after day 20 is essentially flat while the computations show its characteristic concave upward trend.

B-17 (Fig. 72): A calibration time of 15 days was used for this run. Like F-22 this run had no late additions of aluminum and its starting level was essentially the same as F-22's. There appears to be one bad aluminum data point on day 20 that should probably be disregarded. Like F-22 and other runs the computed prism velocities between days 30-40 are below the measured values. As before, it appears to be caused by the aluminum face velocity correction factor used in the model. Although the pyramid velocities don't look bad, closer examination shows that the predicted velocities are generally low between days 20-30 and high after that. The computed aspect ratio is very near that of the final value but the data reaches its final level more quickly than the computed one does.

C-49 (Fig. 73): A calibration time of 30 days was used for this run. This late time was used because of the behavior of the side 2-pyramid face. This is the run in which the side-2 pyramid face essentially disappeared and resulted in a large step change in face velocity. Since the magnitude of the step change is not currently calculable, using a calibration time prior to this step would lead to results that had no chance of following the side 2 faces. Like runs F22 and B-17 this run had no late additions of aluminum; however, its starting aluminum levels was one-half that of these other two runs. Face velocities were generally well tracked by calculations during the last 20 days of the run; however, the calculations indicated an increasing aspect ratio during the last 20 days while the actual data show a level value.

E-21 (Fig. 74): A calibration time of only 10 days was used for this run. This early time was used since the run only lasted 30 days. This run was unique in that it had no EDTA and no aluminum and it produced a very short, squat crystal that reached the edge of the growth platform at a considerably lower mass (200 kg) and thus higher temperature (~40^{o}C) than the other runs. The computed velocities did a good job in matching measured growth rates. However, because of the limited growth temperatures the range of velocities was much less than is generally seen in a typical run. An exception to the good fit is the blip in computed velocities right at the end of the run. This is driven by the jump in supersaturation that resulted from a steeper drop than normal in growth-solution temperature. This might suggest that the squared dependence on supersaturation is too strong. However, the data gap between days 24-29 makes this interpretation somewhat speculative.

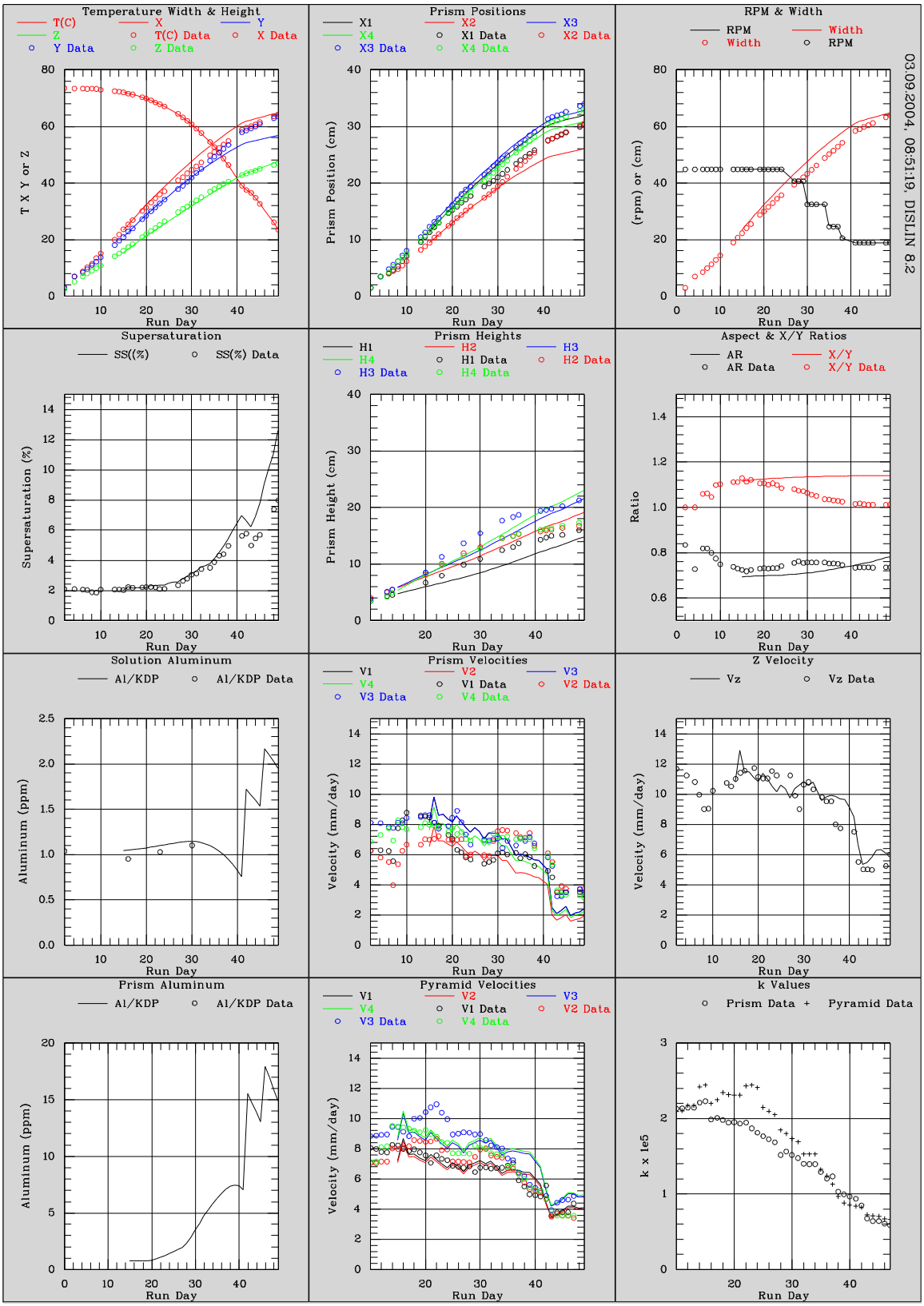

Figure 66. B-15 extrapolated from 15 days.

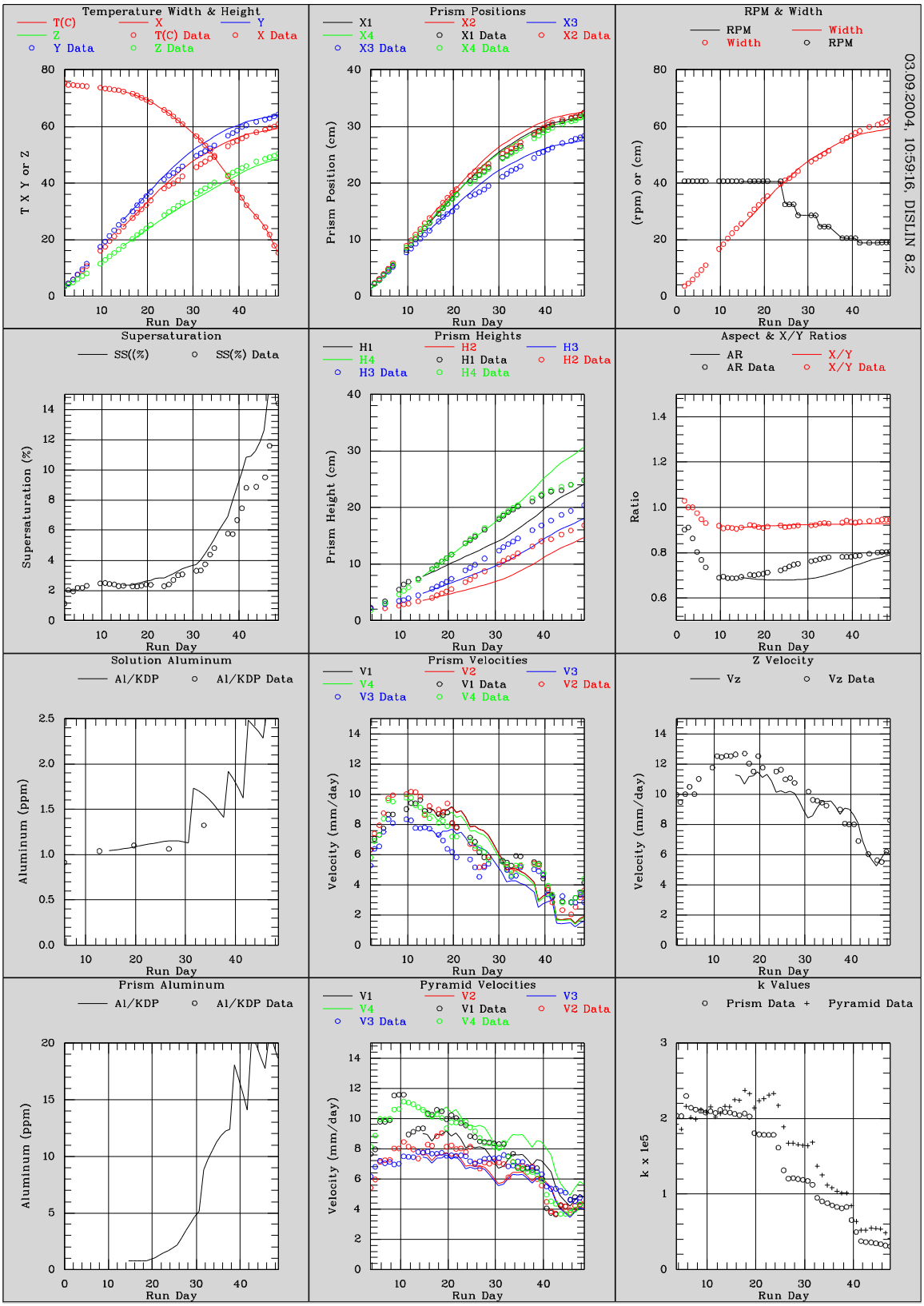

Figure 67. F-21 extrapolated from 15 days.

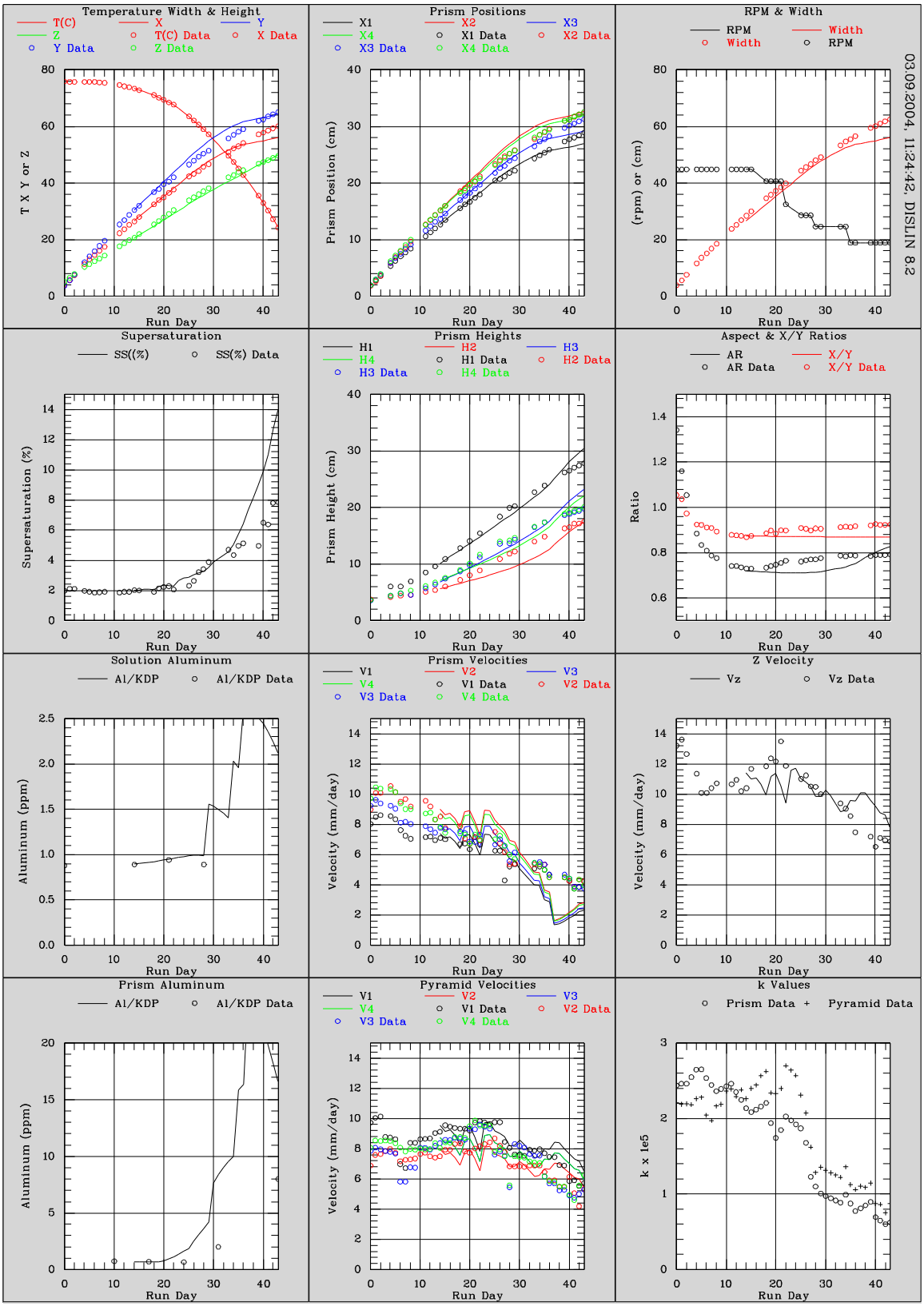

Figure 68. C-47 extrapolated from 15 days.

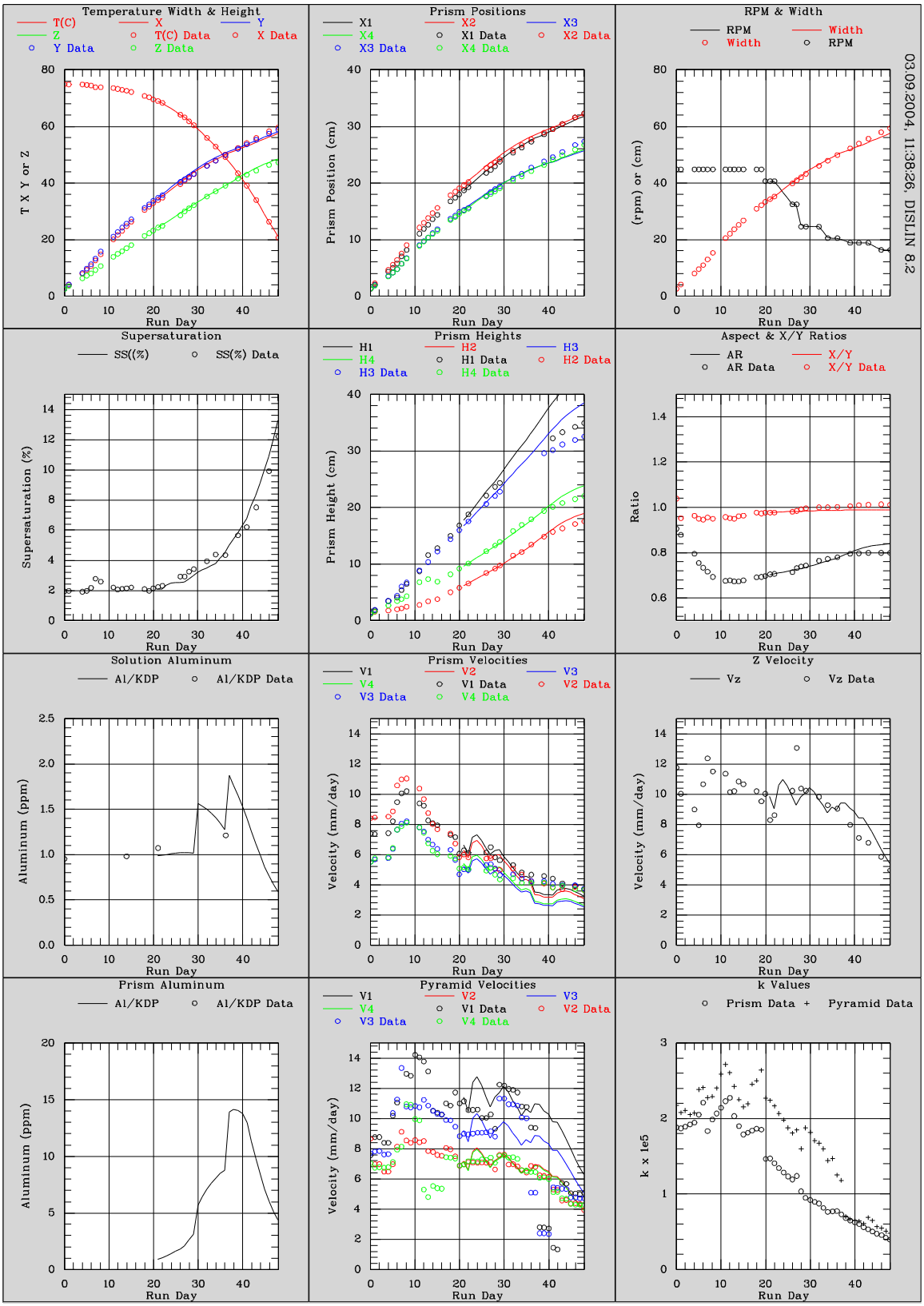

Figure 69. E-17 extrapolated from 20 days.

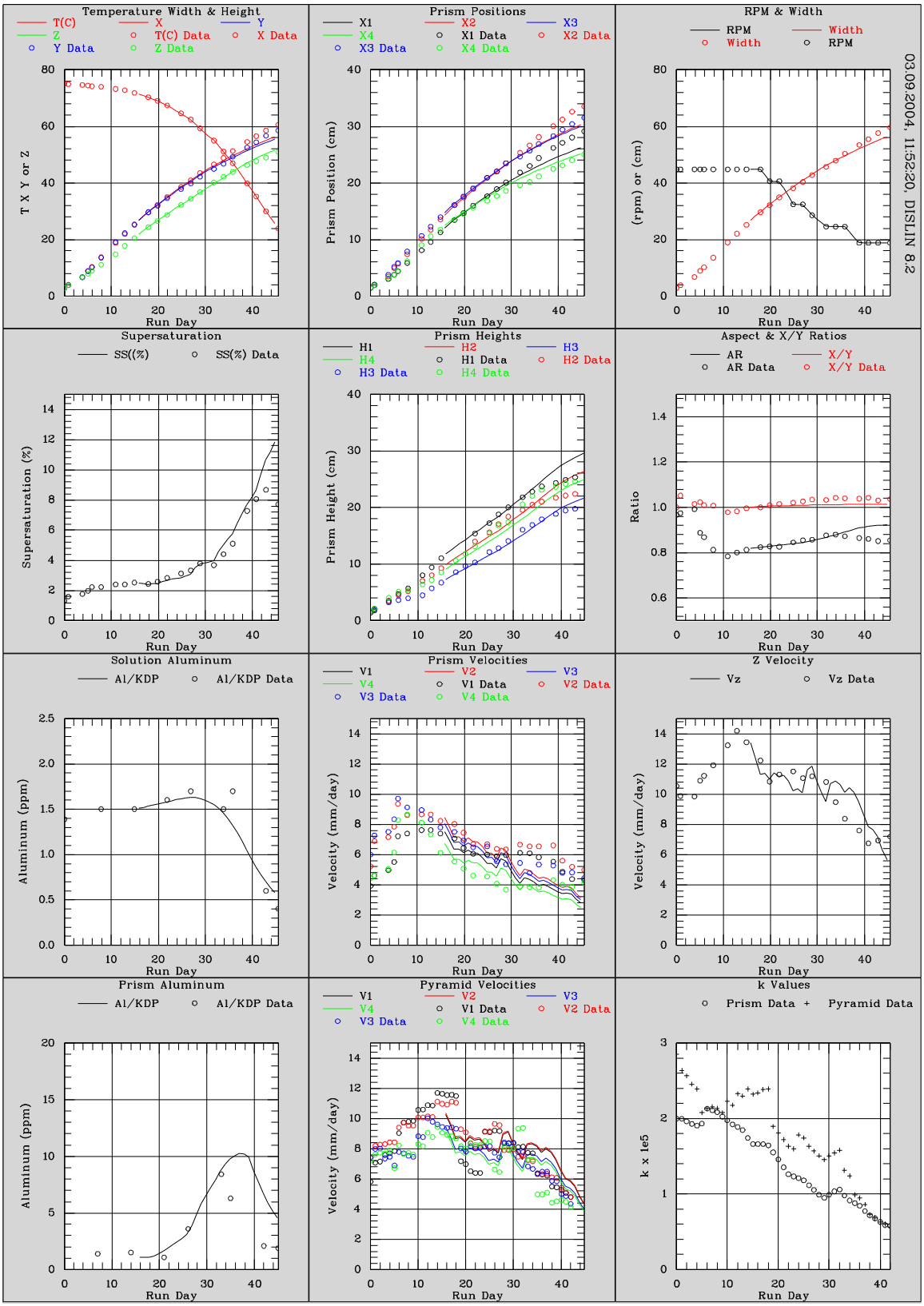

Figure 70. F-22 extrapolated from 15 days.

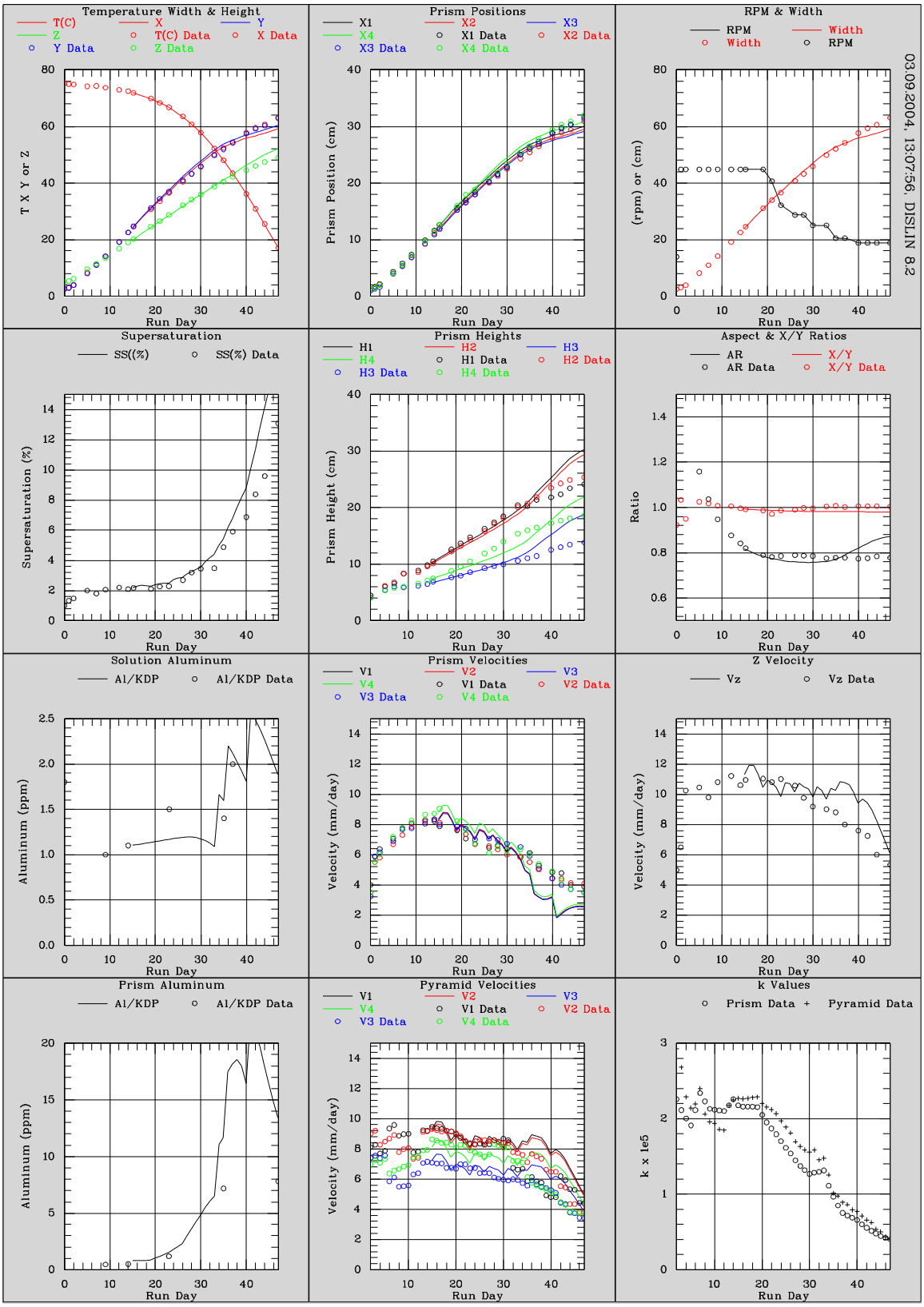

Figure 71. C-48 extrapolated from 15 days.

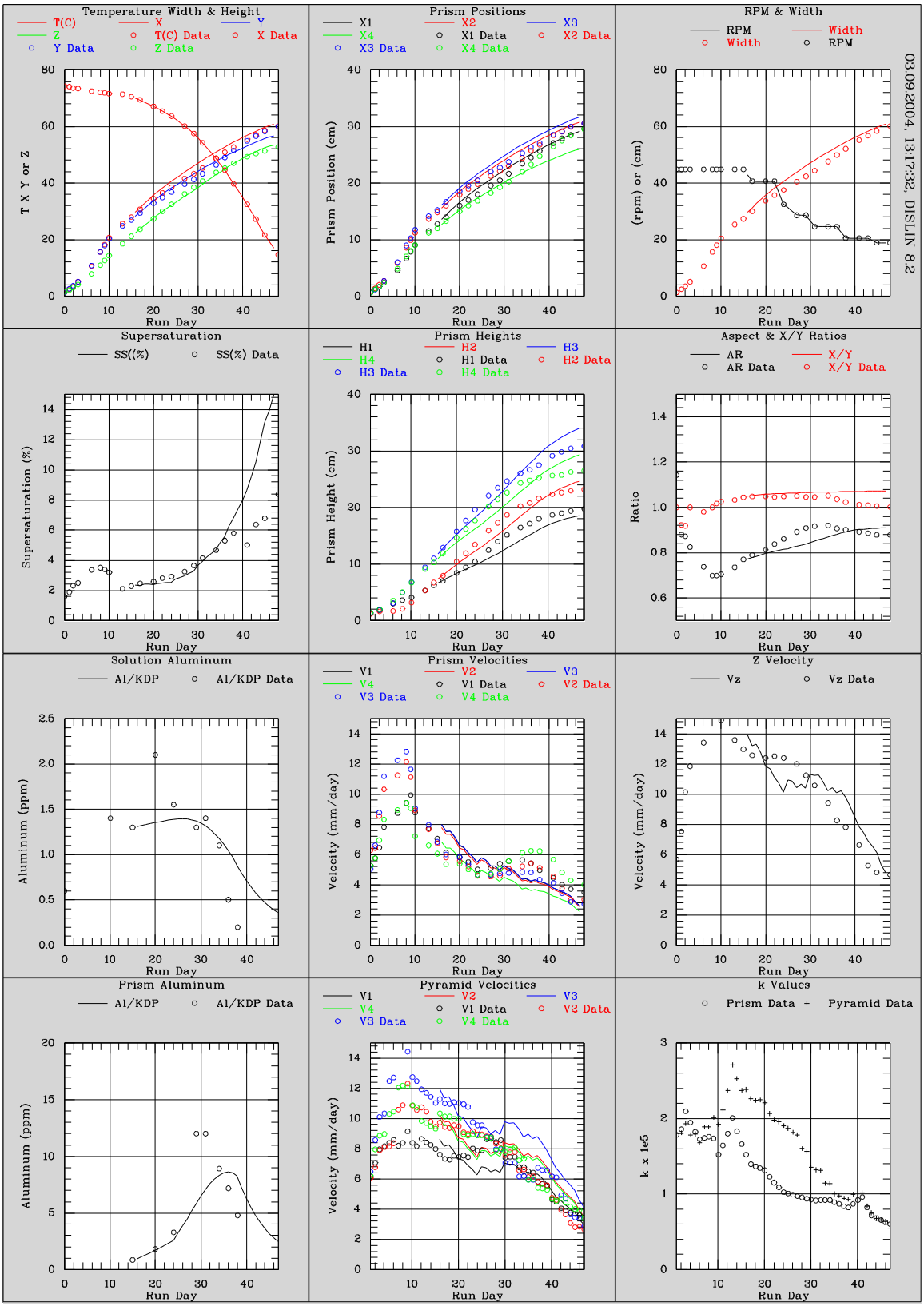

Figure 72. B-17 extrapolated from 15 days.

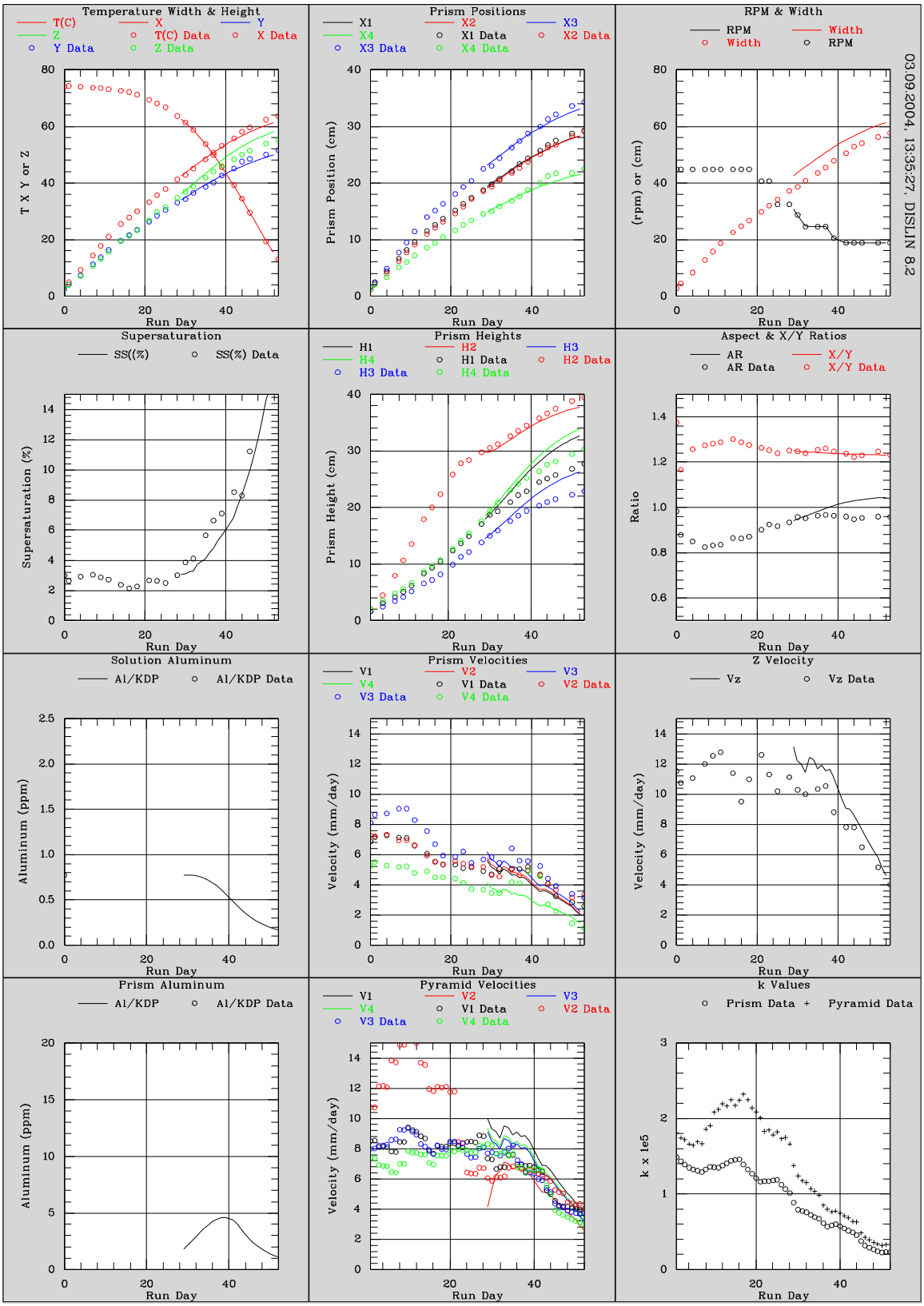

Figure 73. C-49 extrapolated from 28 days.

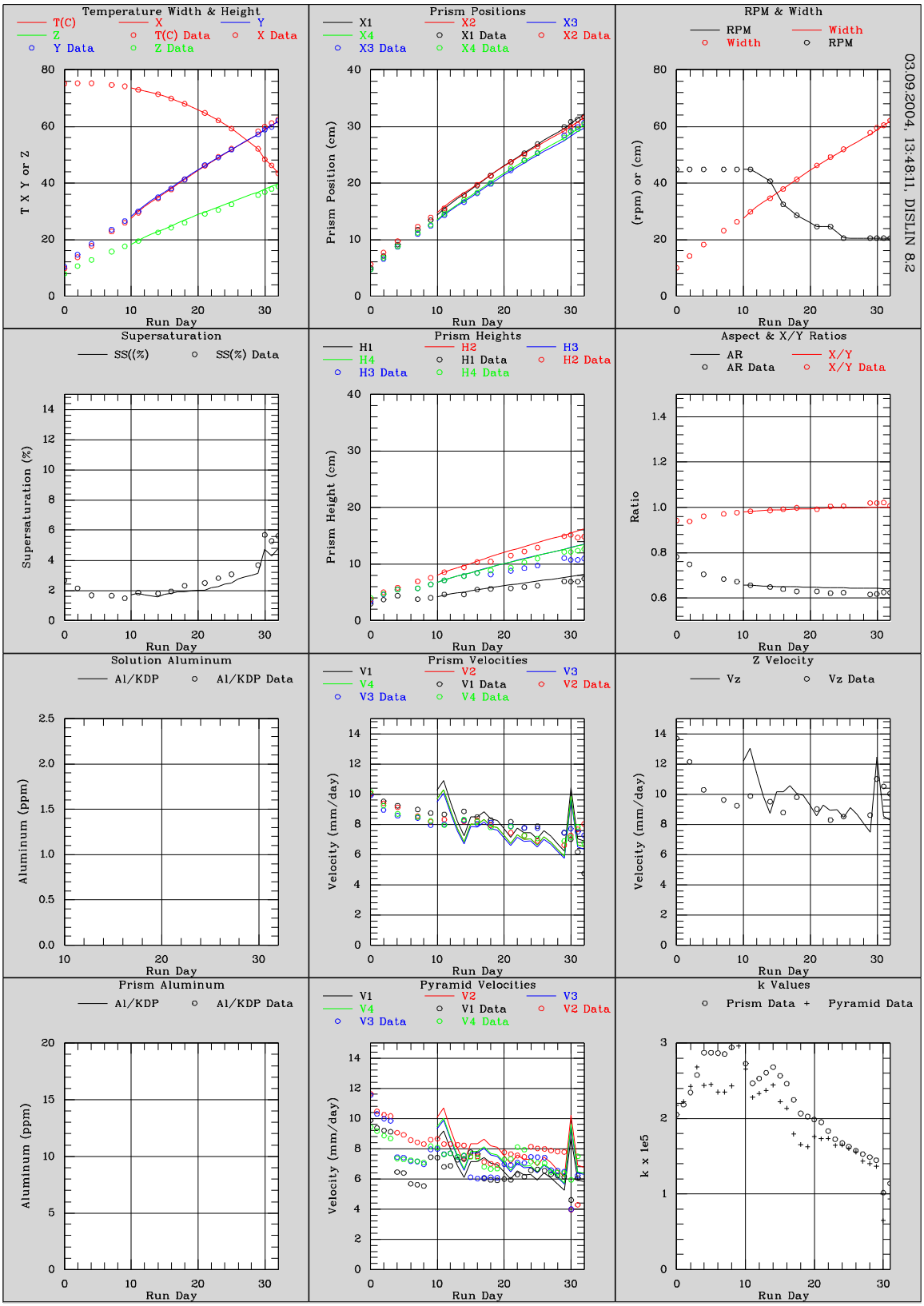

Figure 74. E-21 extrapolated from 10 days.

CONCLUSIONS

We find that during the growth of large KDP crystals in lined growth tanks the shape of the crystal often changes little after the first 10 days or so. On the other hand, a considerable run-to-run variability in crystal shape has been seen that cannot easily be attributed to differences in operating parameters. We find that this variability in shape can be attributed to relatively small, 10-15%, differences in velocities of the individual faces. This variability appears to be random. We believe it is driven by inherent differences in growth-center (dislocation) strength. The variability seen in large boule face-growth rates is less than we have recently observed in small-scale kinetic experiments. This natural variability makes it very difficult to determine how a change in operating procedure influences final crystal shape if the results of only a few runs are available. For example, we found that a 10% random variation in face growth rates can yield crystals with aspect ratios running from 0.62 – 0.96 within a twelve crystal sample.

Once established relative growth-center strengths persist and result in constant crystal shapes with time. This fact allows meaningful estimates of final shape and plate yield to be made based on early data. We estimate that after 15 days we should be able to estimate final yield with an average accuracy of ±30%. These estimates are based on using a kinetic based model to compute final crystal shapes from initial growth information. Comparisons of predictions from these extrapolations to actual data indicate that the model is only approximate. The data suggests the aluminum retardation model needs some improvement. In addition, recent data from runs and other experiments indicate that mass transfer as well as kinetics plays a role in the growth process. With an improved extrapolation model we believe early yield estimates could be substantially improved.

ACKNOWLEDGEMENTS

Many individuals contributed to the reported work. At LLNL they include Paul Ehrmann, Keith Kishiyama, Marcus Monticelli, Dave Lens, Phil Miller, and Sandy Anderson. We are indebted to James Bell and Lawrence Hand at NASA Ames for their hard work on measuring transport rates in a half-scale model system.

REFERENCES

1. L.N. Rashkovich, KDP- Family single crystals, The Adam Hilger series on optics and optoelectronics, New York, 1991. See references within.

2. P.G. Vekilov, Yu.G. Kuznetsov, A.A. Chernov, J. Crystal Growth v121, 184 (1992).

3. Recovery of surfaces from impurity poisoning during crystal growth, T.A. Land, T.L. Martin, S. Potapenko, G.T.R. Palmore, J.J. DeYoreo, Nature, Vol. 399, 442 (1999).

4. A comparison of growth hillock structure and step dynamics on KDP{100} and {101} surfaces using force microscopy, T.A. Land, J.J. DeYoreo, T.L. Martin, G.T.R. Palmore, Crystallography Reports, Vol. 44, No.4, 9 (1999).

5. The effect of dislocation cores on growth hillock vicinality and normal growth rates of KDP {101} surfaces, J. J. De Yoreo, T. A. Land, L. N. Rashkovich, T. A. Onischenko, J. D. Lee, O. V. Monovskii, and N. P. Zaitseva, Journal of Crystal Growth, v182 N3-4, 442 (1997).

6. Limits on surface vicinality and growth rate due to hollow dislocation cores on KDP {101}, J.J. DeYoreo, T.A. Land, J. D. Lee, Physical Review Letters, 78, 4462 (1997).

7. Growth morphology of vicinal hillocks on the {101} face of KH2PO4: from step-flow to layer-by-layer growth, J.J. DeYoreo, T.A. Land, B. Dair, Physical Review Letters, 73(6), 838 (1994).

8. DeYoreo, J.J., Orme, C.A., and Land, T.A., "Using atomic force microscopy to investigate solution crystal growth", In: Advances in crystal growth research, Eds: Sato, K., Nakajima, K., and Furukawa, Y., (Elsevier Science, Amsterdam), 2001.

9. H.F. Robey, S.Yu. Potapenko, K.D. Summerhays, J. Crystal Growth, v213, 355 (2000).

10. H.F. Robey, S.Yu. Potapenko, K.D. Summerhays, J. Crystal Growth, v213, 340 (2000).

11. H.F. Robey, D. Maynes, "Numerical simulation of the hydrodynamics and mass transfer in the large scale, rapid growth of KDP crystals. Part 1: Computation of the transient, three-dimensional flow field," J CRYST GROWTH 222 (1-2): 263-278 JAN 2001

12. KDP/DKDP crystallizer headspace temperatures, C.B. Thorsness, K. Kishiyama, J. Kimmons and T.A. Land, NIF002383, (2003).

13. Dylla-Spears, R. Memo, NIF0110923 "Progress on CFD Component of LDRD 03-ERD-051" (September 23, 2003)

14. Robey, HF "Numerical simulation of the hydrodynamics and mass transfer in the large scale, rapid growth of KDP crystals. Part 2: Computation of the mass transfer," J CRYST GROWTH 259 (4): 388-403 DEC 2003.

Memos relating to LDRD work:

P. E. Miller, "Some equilibria aspects of KDP growth solutions", LLNL internal memo NIF0101124, Mary 20, 2003. Official Use Only, Not for Publication or Reproduction.

P. Ehrmann, R. Dylla-Spears and T. Land, "20 L Tank aluminum incorporation study", LLNL internal memo NIF0106454, July 7, 2003.

C.B. Thorsness, "Supersaturation estimates during KDP large crystal growth", LLNL internal memo NIF0108354, July 10, 2003.

C.B. Thorsness, "Large supersaturation increases near the end of KDP rapid growth runs", LLNL internal memo NIF0107085, July 17, 2003.

C.B. Thorsness, "Preliminary modeling results for KDP large crystal runs B-15, C-46, C-47, E-15, E-17 and F-21", LLNL internal memo NIF0110148**AB-Rev 2**, October 1, 2003.

C.B. Thorsness, "Z-Growth at the End of KDP Run E-21", LLNL internal memo NIF0110879, May 4, 2004.

C.B. Thorsness, "Z-Growth at the End of KDP Run E-21" LLNL internal memo NIF0110879, May 7, 2004.

Paul Ehrmann, Terry Land, Rebecca Dylla-Spears and Chuck Thorsness, "Aluminum uptake by large KDP crystals", *NIF0110915 revAB*, June 4, 2004.

Paul Ehrmann, Terry Land, Rebecca Dylla-Spears, Sandy Anderson and C.B. Thorsness, "Aluminum uptake by large KDP boules in the absence of EDTA", LLNL internal memo NIF0111075, June 11, 2004.

Sandra Anderson, Phil Miller and C.B. Thorsness, "Growth Kinetics of KDP at 40^{o}C", LLNL internal memo, June 14, 2004.

Paul Ehrmann, Terry Land, Rebecca Dylla-Spears, and C.B. Thorsness, "B-20 KDP Boule Dissolution Experiments.

S. Anderson, C. Thorsness and P. Miller, "Growth Kinetics of KDP", LLNL internal memo NOF0111193, August 25, 2004.

C.B. Thorsness, Terry Land and Paul Ehrmann, "E-22: Influence of Rotation Changes on Growth of a Large KDP Crystal", LLNL internal memo NIF0111677, November 18, 2004.

C.B. Thorsness, Paul Ehrmann, Terry Land, Patrick McMurtry and Marcus Monticelli, "M-7 – Growth of a KDP Crystal in a 1500L Tank Using Low Rotational Speeds", LLNL internal memo NIF0112490, June 2, 2005.